Intrinsic Predictability of the 20 May 2013 Tornadic Thunderstorm Event in Oklahoma at Storm Scales

YUNJI ZHANG

Laboratory for Climate and Ocean–Atmosphere Studies, Department of Atmospheric and Oceanic Sciences, School of Physics, Peking University, Beijing, China, and Department of Meteorology, The Pennsylvania State University, University Park, Pennsylvania

FUQING ZHANG AND DAVID J. STENSRUD

Department of Meteorology, The Pennsylvania State University, University Park, Pennsylvania

ZHIYONG MENG

Laboratory for Climate and Ocean–Atmosphere Studies, Department of Atmospheric and Oceanic Sciences, School of Physics, Peking University, Beijing, China

(Manuscript received 20 March 2015, in final form 22 December 2015)

ABSTRACT

Using a high-resolution convection-allowing numerical weather prediction model, this study seeks to explore the intrinsic predictability of the severe tornadic thunderstorm event on 20 May 2013 in Oklahoma from its preinitiation environment to initiation, upscale organization, and interaction with other convective storms. This is accomplished through ensemble forecasts perturbed with minute initial condition uncertainties that were beyond detection capabilities of any current observational platforms. It was found that these small perturbations, too small to modify the initial mesoscale environmental instability and moisture fields, will be propagated and evolved via turbulence within the PBL and rapidly amplified in moist convective processes through positive feedbacks associated with updrafts, phase transitions of water species, and cold pools, thus greatly affecting the appearance, organization, and development of thunderstorms. The forecast errors remain nearly unchanged even when the initial perturbations (errors) were reduced by as much as 90%, which strongly suggests an inherently limited predictability for this thunderstorm event for lead times as short as 3–6 h. Further scale decomposition reveals rapid error growth and saturation in meso-γ scales (regardless of the magnitude of initial errors) and subsequent upscale growth into meso-β scales.

1. Introduction

Severe convective thunderstorms, with their wind gusts, lightning strikes, torrential rain, hail, and sometimes tornadoes, have been recognized as one of the most dangerous weather hazards threatening human lives and property. For the past 70 years, the National Weather Service (NWS) of the United States issued hazardous weather warnings through a paradigm of ''warn-on-detection,'' which was primarily based on the detection of certain weather phenomena, including radar observations, environmental conditions, and spotters' reports (e.g., Coleman et al. 2011; Brotzge and Donner 2013). Owing to the deployment of a nationwide Doppler weather radar network, warning lead time has increased due to both increasing probability of detection (POD) and decreasing false alarm ratio (FAR). For example, the lead time for tornado warnings has increased from 3 min in 1978 to 14 min in 2011 (Stensrud et al. 2009, 2013).

Further extending tornado warning lead time beyond approximately 17 min using the current paradigm may be difficult (Stensrud et al. 2013). However, observation platforms, numerical weather prediction (NWP) models, data assimilation algorithms, and computational resources have progressed considerably in recent

Corresponding author address: Zhiyong Meng, Laboratory for Climate and Ocean–Atmosphere Studies, Department of Atmospheric and Oceanic Sciences, School of Physics, Peking University, 209 Chengfu Rd., Haidian District, Beijing 100871, China.
E-mail: zymeng@pku.edu.cn

DOI: 10.1175/MWR-D-15-0105.1

years. Since Snyder and Zhang (2003) incorporated radar observations in NWP models using an ensemble Kalman filter (EnKF) approach, convection-allowing (horizontal grid spacing of ~1 km) ensemble forecasts with initial conditions (IC) combining high-resolution in situ observations via ensemble-based data assimilation techniques (e.g., EnKF) have proven to be helpful in providing warning guidance (Roebber et al. 2004; Stensrud et al. 2009, 2013). For example, the annual "Spring Experiment" of NOAA's Hazardous Weather Testbed (HWT) has focused upon applying state-of-the-art convection-allowing ensemble predictions to severe weather forecasts in recent years (e.g., Coniglio et al. 2010; Johnson et al. 2011a,b, 2014; Clark et al. 2012; Johnson and Wang 2013; Karstens et al. 2015). Numerous case studies have also proven the reliability of high-resolution short-range ensemble forecasts for predicting convective storms (Hawblitzel et al. 2007; Stensrud and Gao 2010; Dawson et al. 2012; Snook et al. 2012; Wheatley et al. 2014; Yussouf et al. 2013, 2015). A transition from warn-on-detection to "warn-on-forecast" is believed to be one potential future for severe weather warning (Stensrud et al. 2009, 2013). An important question to ask is how far warning lead times can be extended in this paradigm.

This question is brought forward as some studies pointed out that the positive impact of data assimilation might be lost within a short time. For example, Aksoy et al. (2010) using EnKF assimilation of radar radial velocity and reflectivity found that equitable threat score (ETS) decreased by more than 50% within 20 min of the ensemble forecast for all three cases studied. A similar finding was obtained by Gasperoni et al. (2013) using a 3DVar assimilation of synthetic radar refractivity observations under an observing system simulation experiment (OSSE) framework, who concluded that for an imperfect model the forecast errors might overwhelm the positive impact of data assimilation in 30–60 min. These results highlight the limited intrinsic predictability of some convective storms.

Atmospheric predictability, first proposed in Lorenz (1963), can be broadly divided into two types (Lorenz 1996; Melhauser and Zhang 2012). One is practical predictability, or the predictability given current capability, which is primarily limited by realistic errors in forecast models and initial conditions (Lorenz 1982, 1996). The other aspect, intrinsic predictability, is the longest possible forecast extent given *nearly* perfect atmosphere estimations and forecast models (Lorenz 1969). The examination of intrinsic predictability was often performed using an "identical twin experiments" method in which two (or more) simulations employed an identical numerical model but slightly, observationally indistinguishable, different ICs. Based on the examination of upscale error growth within idealized moist baroclinic waves and complimentary to earlier studies on the forecast error growth of a winter snowstorm in Zhang et al. (2002, 2003), a generalized conceptual model of how mesoscale intrinsic predictability becomes limited was presented in Zhang et al. (2007). In this model, initial errors that were very small in amplitude grew and saturated at convective scales and rapidly spread throughout the integration domain, then the upscale transfer of errors into mesoscale and synoptic scale would limit the predictability of these scales. This conceptual model was proved by Hohenegger and Schär (2007b) and recently reexamined by Selz and Craig (2015) using a convection-allowing model. Differentiated underlying dynamics in limiting intrinsic versus practical predictabilities were also proved by Leoncini et al. (2010) that examined growth of initial errors that spans two orders of magnitudes.

The nonlinear upscale growth of small initial errors through moist convection were observed in several warm-season case studies (e.g., Zhang et al. 2006; Bei and Zhang 2007; Hohenegger and Schär 2007a,b). Melhauser and Zhang (2012) revealed that a reduction of initial perturbations might not bring a corresponding linear decrease of forecast errors in bow echoes, while a more linear relationship was obtained in the squall-line study of Wu et al. (2013). In Van Sang et al. (2008), random perturbations of $\pm 0.5\,\mathrm{g\,kg^{-1}}$ in moisture resulted in different structures of an idealized tropical cyclone (TC). The TC predictability was found to be more limited with larger vertical wind shear (Zhang and Tao 2013), and small changes in IC may suppress a Gulf low from intensifying into a tropical storm (Zhang and Sippel 2009). The large impact of moisture on mesoscale gravity waves was also shown by Wei and Zhang (2014). An independent relationship between error growth and the complexity of microphysical parameterization schemes was found by Wang et al. (2012), suggesting the intrinsically nonlinear nature of error growth in moist dynamics. Other studies indicate that growth of perturbations in large scales and the downscale transition might be dominant under certain synoptic phenomena (e.g., Durran et al. 2013; Durran and Gingrich 2014; Johnson et al. 2014), furthering the difficulty in estimating intrinsic predictability limitations.

Much of the work on intrinsic predictability has been focused on meso-α or meso-β systems such as winter storms, MCSs, or TCs, while studies of local severe convective thunderstorms on the meso-γ scale [2–20 km

(Orlanski 1975), e.g., single cell and supercell storms] have focused more on practical rather than intrinsic predictability. Cintineo and Stensrud (2013) found that with current analysis uncertainty, supercell location was predictable out to 2 h, while mesocyclone location was only predictable out to 40 min. Using datasets from the Spring Experiment, Surcel et al. (2014, 2015) concluded that none of the examined prediction systems showed any practical predictability in meso-β- and meso-γ-scale precipitation beyond 2–3 h. Our recent study (Zhang et al. 2015, hereafter Z15) explored the practical predictability of the tornadic thunderstorm event on 20 May 2013 in Oklahoma that spawned one of the most disastrous tornadoes in recent years. We found that the initiation, development, and organization of convection on that day were strongly modulated by PBL evolution during the diurnal cycle, and that topography could also have dynamical impacts beyond simply altering the environmental conditions.

Understanding the intrinsic predictability of severe convective storms is essential in exploring the appropriate time scale for which the warn-on-forecast paradigm is applicable and reliable. As a follow up of Z15, this paper examines how tiny initial uncertainties affect the initiation and development of severe thunderstorms in an ensemble framework utilizing a convection-allowing NWP model applied to the same severe weather event. The model configuration and method of generating initial perturbations are presented in section 2. Sections 3 analyzes the control ensemble forecast, and section 4 explores the sensitivity of the ensemble forecasts to the magnitude and structure of initial uncertainties. A detailed analysis of two specific ensemble members is presented in section 5, and a summary is provided in section 6.

2. Experiment design

a. Model description

The numerical model used is version 3.5 of the fully compressible nonhydrostatic WRF Model (Skamarock et al. 2008), the same as in Z15, with four domains of 201 × 121, 256 × 175, 316 × 244, and 400 × 301 horizontal grid points of 27-, 9-, 3-, and 1-km grid spacing, respectively, with 61 terrain-following hydrostatic-pressure vertical levels in all domains and 18 levels in the lowest 1 km AGL. The largest domain covered the entire United States, while the innermost domain covered most of Oklahoma (Fig. 1). In Z15, four domains were initialized at 1200 UTC 19 May, 1200 UTC 20 May, 1200 UTC 20 May, and 1500 UTC 20 May, respectively, and integrated separately to 0000 UTC 21 May. The IC and LBCs were provided by 1200 UTC 19 May GFS analysis and subsequent forecast for the outermost domain and their respective parent domains for each inner domains with no feedback (i.e., one-way nesting). Physical parameterization schemes applied included Thompson microphysics (Thompson et al. 2008); Grell 3D ensemble cumulus (Grell and Dévényi 2002), which was only applied in the 27-km domain; MM5 similarity surface layer (Zhang and Anthes 1982); RUC land surface (Benjamin et al. 2004); Mellor–Yamada–Nakanishi–Niino (MYNN) level-2.5 PBL (Nakanishi and Niino 2009); RRTM longwave radiation (Mlawer et al. 1997); and Goddard shortwave radiation schemes (Chou and Suarez 1994). Simulated radar reflectivity was calculated using the built-in module of the Thompson microphysics scheme with condensates of cloud water, rainwater, cloud ice, snow, and graupel.

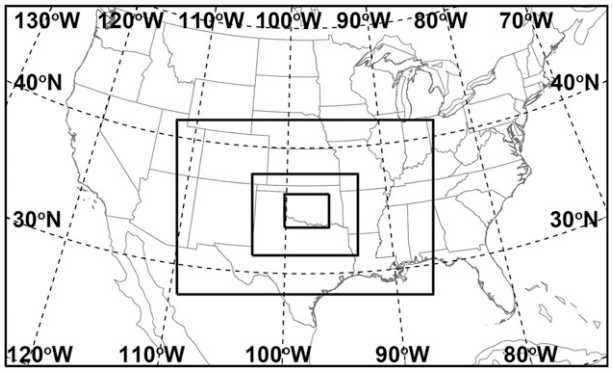

FIG. 1. Model domain configuration with the entire figure being the geographical coverage of D01 and inner solid rectangles representing D02, D03, and D04.

b. Ensemble generation

To generate tiny initial ensemble perturbations in a flow-dependent manner, an additional domain with horizontal grid spacing of 250 m was implemented. This domain covered nearly the entire 1-km domain, within 10-km distance (i.e., 10 1-km grid points) from each boundary. Because the grid spacing of this domain was finer than 1 km, the PBL parameterization scheme was turned off,[1] diffusion was used for vertical mixing, and a

[1] This experiment falls into the range of large-eddy-permitting (LEP) simulations as termed by Green and Zhang (2015) given that the resolution is still too coarse to be classified as a true large-eddy simulation (LES).

TABLE 1. Statistics of the EF_PERT, EF_TINY, EF_1900, and EF_2000 ensembles and initial difference between members 13 and 17 of EF_PERT.

		T (K)	Q_v (g kg^{-1})	U (m s^{-1})	V (m s^{-1})
EF_PERT	Std dev	0.066	0.11	0.19	0.20
(1715 UTC)	Max dev	3.2	7.5	5.9	6.9
EF_TINY	Std dev	0.0082	0.014	0.024	0.025
(1715 UTC)	Max dev	0.98	3.5	2.1	1.7
EF_1900	Std dev	0.037	0.065	0.14	0.13
(1915 UTC)	Max dev	8.6	11	17	12
EF_2000	Std dev	0.049	0.071	0.18	0.18
(2015 UTC)	Max dev	18	10	31	27
EF_PERT	RMS difference	0.039	0.090	0.085	0.087
Members 13 and 17 (1705 UTC)	Max difference	1.48	5.3	5.2	3.0

prognostic 1.5-order turbulent kinetic energy (TKE) closure was applied for a three-dimensional turbulence parameterization. After the initialization of the 1-km domain at 1500 UTC 20 May, the extra 250-m domain was added at 1700 UTC (when there was no simulated radar reflectivity) with two-way nesting and integrated for 6 h, with output files created every 2.5 min together with those from its parent 1-km domain. Then, for a given output time, several realizations were generated by replacing variable values on all the 1-km grids by those randomly selected values from the surrounding 250-m grid points within a certain radius from the 1-km grid point (here the radius was set to 1 km). For each set of realizations that was generated from one pair of 250-m and 1-km output files, their mean values were subtracted from each of them and the remaining ''perturbations'' were added back to the 1700 UTC 1-km output as initial conditions for ensemble forecast. Five variables were ''perturbed,'' including the three components of wind, potential temperature, and water vapor mixing ratio. A total of 60 ensemble members using 15 (total) 250-m outputs from 1712:30 to 1747:30 UTC were produced following these procedures, and they were integrated for 6 h to 2300 UTC.

It should be noted that the choice of a 1-km grid spacing for the ensemble forecasts of this study is a compromise between the available computing resources and the ability of the model in representing essential physical processes that are most relevant to the prediction of this event, including midlevel mesocyclones and interactions between cold pools and vertical wind shear, albeit a much higher grid spacing is necessary to properly resolve physical properties of convective flows as shown in Bryan et al. (2003) and Lane and Knievel (2005). The above-described ensemble forecast was denoted as EF_PERT and is the primary focus of this study. A 1-km deterministic forecast was integrated from the 1700 UTC output, which was also the ensemble mean of EF_PERT ICs, to establish a reference simulation in a perfect model scenario without model errors, and this deterministic forecast was referred to as ''CNTL_17Z.'' An additional ensemble (EF_TINY) that was initialized from much smaller initial errors generated by multiplying the original perturbations of EF_PERT by a factor of 0.1 was carried out in order to examine the sensitivity of ensemble performance to the reduction of errors. To explore the sensitivity of ensemble forecast to ICs that were perturbed at different times with corresponding flow-dependent uncertainties, two experiments of EF_1900 and EF_2000 were conducted. The ICs of EF_1900 (EF_2000) were generated following the same manner of EF_PERT but performed at 1900 (2000) UTC by recentering at 1900 (2000) UTC outputs of CNTL_17Z, and only 4 outputs within ±5 min of 1900 (2000) UTC were used instead of 15 for EF_PERT to exclude the influence of fast-evolving convection-active environment as much as possible. The reference perfect model deterministic forecast, denoted as CNTL_19Z (CNTL_20Z), was initialized at 1900 (2000) UTC using 1900 (2000) UTC output of CNTL_17Z to construct the perfect model scenario. Differences between CNTL_19Z (CNTL_20Z) and CNTL_17Z resulted from this interruption of the continuous CNTL_17Z simulation at 1900 (2000) UTC.

Note that because of the adjustment to unbalances in ensemble ICs, the magnitude of initial perturbations changed after model initialization. The statistics of the four ensembles 15 min after initialization (the first output time) for temperature, water vapor mixing ratio, and two components of horizontal wind are shown in Table 1. For the two ensembles initialized at 1700 UTC, only maximum deviations from ensemble mean in EF_PERT were comparable to current observational

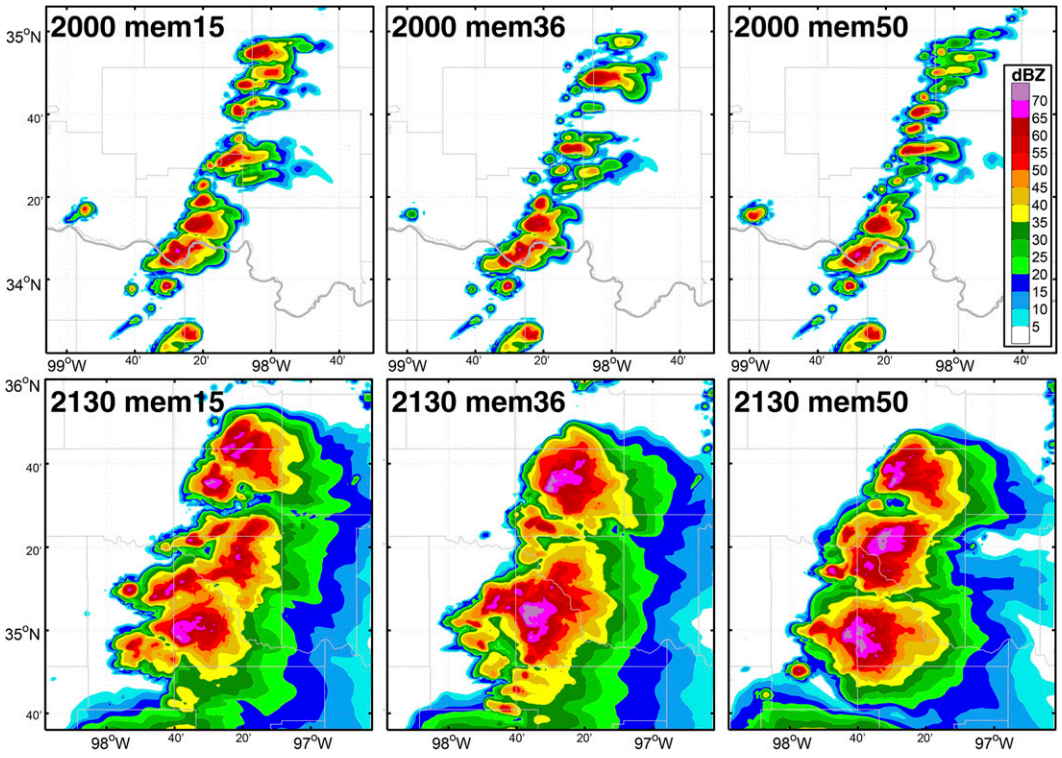

FIG. 2. Composite reflectivity of three randomly selected EF_PERT members at (top) 2000 and (bottom) 2130 UTC. Note that panel regions are different for the two plotted times.

errors and all other statistical parameters had smaller magnitudes, meaning that differences between ICs of ensemble members in EF_PERT were unobservable using current systems, and for EF_TINY those differences were beyond the detection capability of any observational platforms in the foreseeable future. For the EF_1900 and EF_2000 ensembles, the ensemble spreads (standard deviations) were slightly smaller than those of EF_PERT (Table 1), which was due to their perturbations being generated using four outputs. However, the maximum deviations from ensemble mean of these two ensembles were considerably larger than those of EF_PERT (Table 1), which inevitably influenced the performance of the ensemble forecast as shown in section 4.

3. Uncertainties in the simulated storm of the EF_PERT ensemble

a. Radar reflectivity, precipitation, and RMDTE

Figure 2 shows composite reflectivity of 3 out of the 60 ensemble members of EF_PERT at two different times representing early initiation and nearly mature stages, respectively. All ensemble members shared a similar convective organization, a quasi-contiguous line of severe convective storms, and the overall development and morphology were similar to the deterministic forecast of Z15 (their Fig. 4). However, although the convective lines in different members were similar to each other at 2000 UTC, there were differences in the strength and location of single convective cores. The differences in the appearance, development, and organization of each thunderstorm became more apparent during their mature stage at 2130 UTC; for example, member 50 clearly produced three separate convective cells, whereas members 36 had only two cells, and storms in member 15 were much less organized.

Figures 3 and 4 show the ensemble probability of 40-dBZ composite reflectivity values (representing deep convection) during initiation and development, respectively. Convection was first initiated near the Oklahoma–Texas border in several ensemble members at 1900 UTC (Fig. 3a). More cells were triggered later with large differences in location among ensemble members, producing low probabilities that spread out gradually (Figs. 3b,c). The southern segment extended northward with reflectivity probabilities exceeding 50% during early development at 2000 UTC (Fig. 3c),

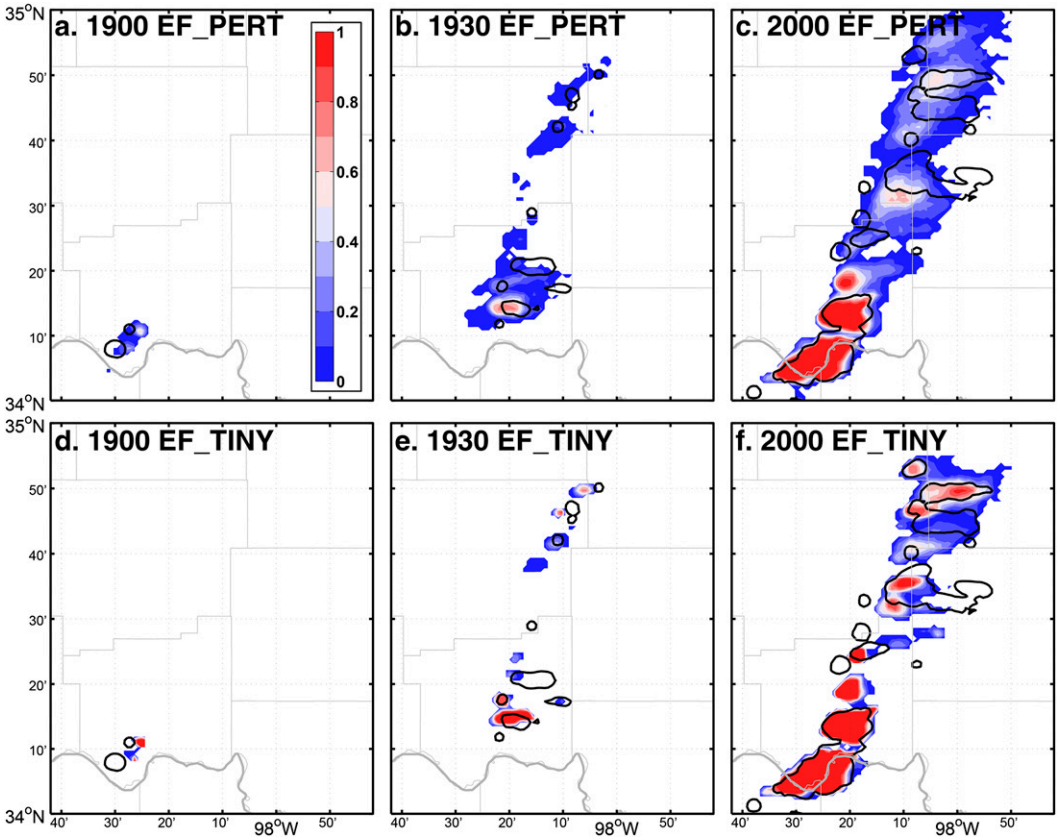

FIG. 3. Ensemble probability of 40-dBZ composite reflectivity (shaded) for (a)–(c) EF_PERT and (d)–(f) EF_TINY at (a),(d) 1900; (b),(e) 1930; and (c),(f) 2000 UTC. Black lines are 40-dBZ composite reflectivity isolines of CNTL_17Z.

indicating the collocation of strong convective storms in the ensemble members. After reaching its strongest linearity around 2100 UTC (Fig. 4a), convection became more discrete and produced lower probabilities connected to areas of higher probabilities (Fig. 4b). The storm in the central region of the convective line dissipated at 2300 UTC (Fig. 4c).

To quantify the degree of storm dislocation among ensemble members, horizontal fractional coverage with respect to ensemble probability (hereafter referred to as "coverage curve") were examined. This metric calculates the horizontal fraction of ensemble probability of a certain variable (e.g., 40-dBZ composite reflectivity) at chosen thresholds. A value of 0 means that at least one ensemble member predicts composite reflectivity larger than 40 dBZ, while a value of 1 means that composite reflectivity exceeds 40 dBZ in all ensemble members. Thus, the slope of the coverage curve when the threshold ranges from 0 to 1 represents the magnitude of divergence between ensemble members; for example, an ensemble with identical members will produce a flat curve since all thresholds produce the same value. In Figs. 5a–c, it is apparent that the coverage curve of the 40-dBZ ensemble probability of EF_PERT became steeper during the forecast, indicating that storms became increasingly dislocated, which is consistent with the development of the ensemble probabilities in Figs. 3 and 4.

Midlevel (2–5 km) updraft helicity (UH) was used to identify convective storms with mesocyclones. Although the 15-min output interval is somewhat coarse, mesocyclone tracks represented by UH values exceeding 180 $m^2 s^{-2}$ [a threshold that performed best in identifying supercells in a 1-km NWP model according to Naylor et al. (2012)] were calculated and were closely collocated with the UH tracks of CNTL_17Z (Fig. 6a). However, there remained large uncertainties in the specific storm locations indicated by the width of UH swaths. Since UH is much smaller in scale compared with radar reflectivity, its coverage curve dropped dramatically between thresholds 0 and 0.1 (Figs. 5d–f). It also shows a decreasing trend at threshold 0 between 2130 and 2230 UTC (Figs. 5e,f) that resulted from storm dissipation (Figs. 4b,c).

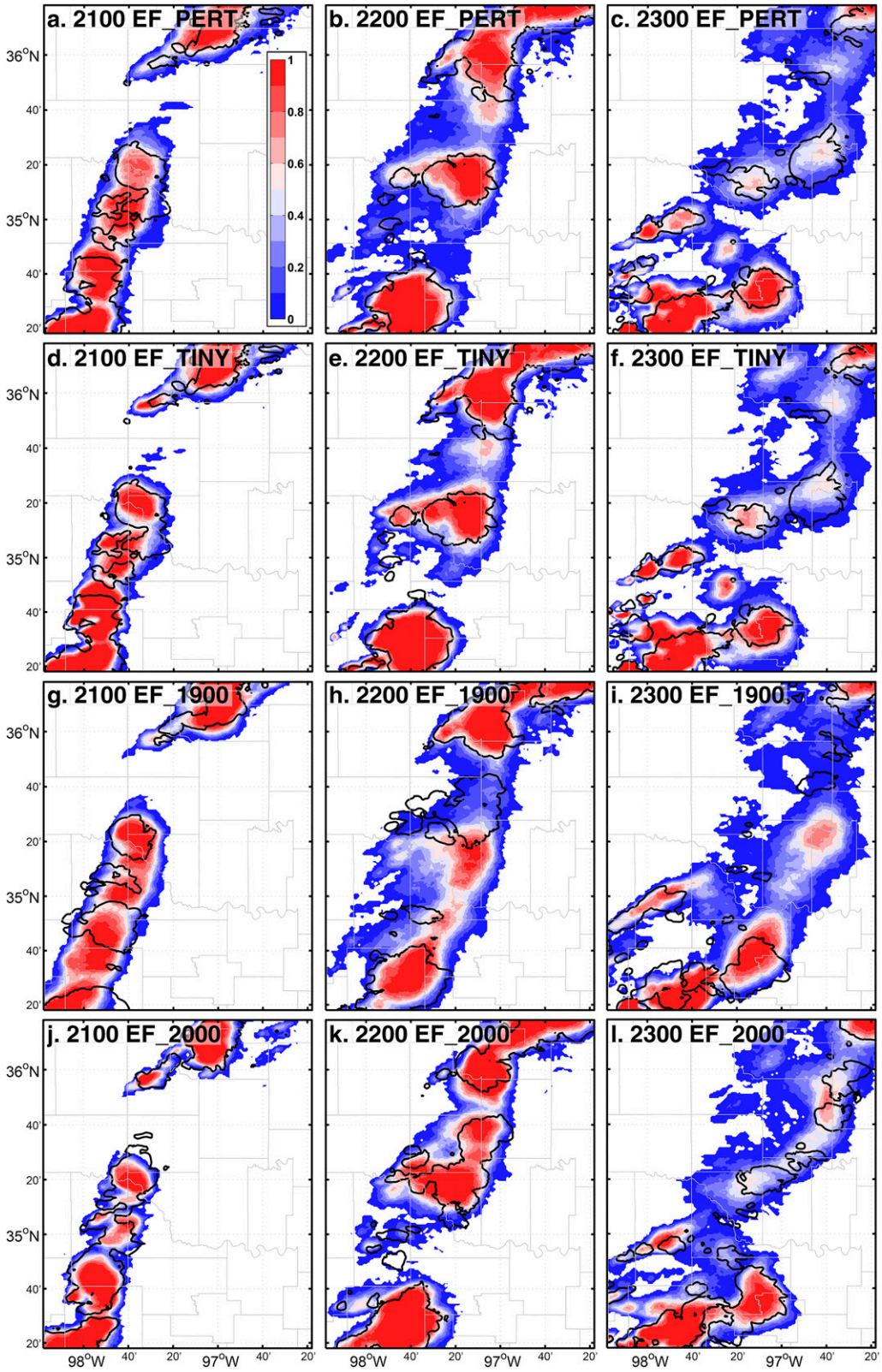

FIG. 4. Ensemble probability of 40-dB*Z* composite reflectivity (shaded) for (a)–(c) EF_PERT, (d)–(f) EF_TINY, (g)–(i) EF_1900, and (j)–(l) EF_2000 at (left) 2100, (middle) 2200, and (right) 2300 UTC. Black lines are 40-dB*Z* composite reflectivity isolines of (a)–(f) CNTL_17Z, (g)–(i) CNTL_19Z, and (j)–(l) CNTL_20Z.

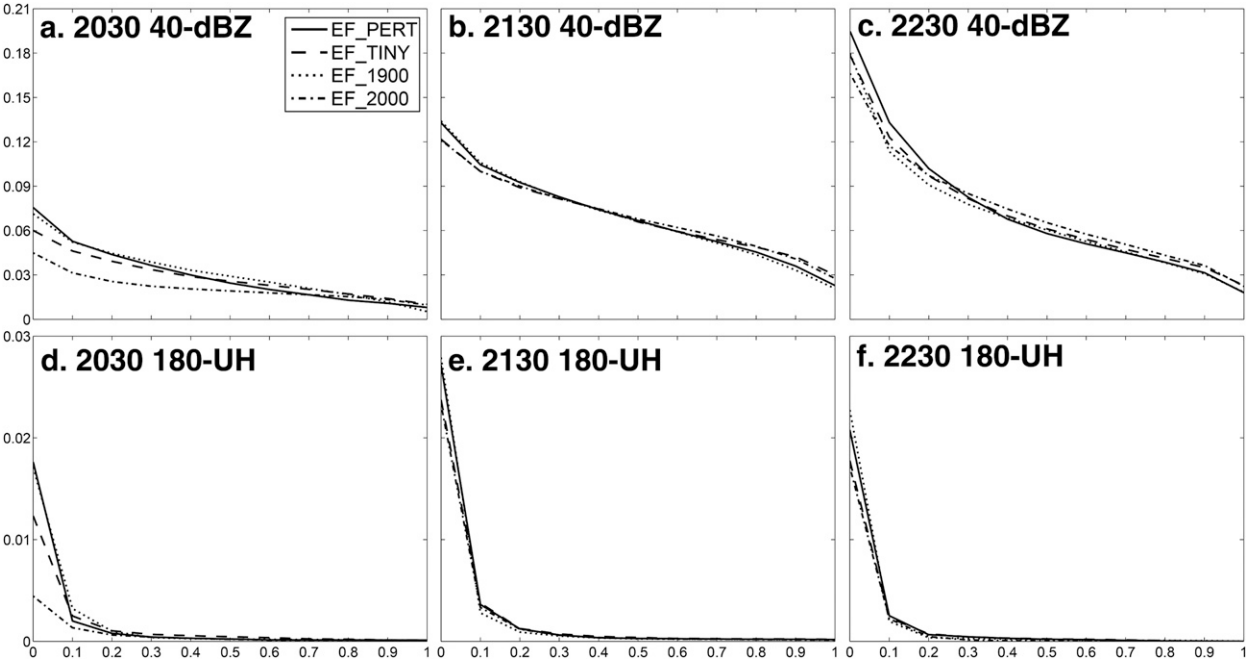

FIG. 5. Coverage curve (see text for explanations) for ensemble probability of (a)–(c) 40-dBZ composite reflectivity and (d)–(f) 180 $m^2 s^{-2}$ updraft helicity (UH) at (a),(d) 2030; (b),(e) 2130; and (c),(f) 2230 UTC for EF_PERT (solid), EF_TINY (dashed), EF_1900 (dotted), and EF_2000 (dotted–dashed).

To quantify the deviation of ensemble members from CNTL_17Z, difference total energy (DTE) following Zhang et al. (2003) was calculated as DTE = (1/2)[u'^2 + v'^2 + (c_p/T_r)T'^2], where c_p = 1004.9 J kg^{-1} K^{-1} is the heat capacity at constant pressure, T_r = 270 K is a reference temperature for calculation, and u', v', and T' were differences between an ensemble member and CNTL_17Z for the two horizontal wind components and temperature at each grid point, respectively. The root-mean difference total energy (RMDTE) was calculated by taking the square root of DTE after it was averaged through a horizontal level, a vertical column, the whole model domain or all the ensemble members. The domain-averaged RMDTE of all members is shown in Fig. 7a; for a reference of RMDTE magnitude, commonly used observational errors of 2 m s^{-1} for horizontal wind components and 2 K for temperature would result in a RMDTE value of approximately 3.4 m s^{-1}. Although convection initiated around 1900 UTC, a rapid increase of RMDTE appeared only after approximately 2000 UTC when convection began to grow upscale, reached a maximum at 2215 UTC and then decreased as convection began to dissipate.

Based on reflectivity and RMDTE features, the ensemble forecast was divided into several stages: pre-CI [(convection initiation) 1700–1900 UTC], CI (1900–2000 UTC), storm development (2000–2215 UTC), and storm dissipation (2215–2300 UTC). Ensemble characteristics during the CI and development stages are examined next.

b. *Environmental conditions for convection initiation*

Convection initiation has long been one of the primary foci of studies on deep moist convection (Schaefer 1986; Johns and Doswell 1992; Weckwerth et al. 2004; Weckwerth and Parsons 2006; Wilson and Roberts 2006) and has proven to be essential to the organization and development of convective storms (Z15). However, accurate prediction of CI remains a challenging problem (Markowski and Richardson 2010; Kain et al. 2013; Burghardt et al. 2014). Here we primarily focus on moisture and instability, two of the basic ingredients for deep moist convection (Johns and Doswell 1992; Doswell et al. 1996), and examine the impact of initial perturbations on these environmental conditions and the potential influence on CI in an ensemble forecast perspective rather than being viewed from the physical processes that trigger convection.

Abundant northward moisture transport on this day originated from the Gulf of Mexico (refer to Z15 for a more detailed description of the synoptic conditions) and helped produce a strong southwest–northeast-oriented dryline across the middle of the domain. The strength of the dryline was indicated by the horizontal gradient in mass-weighted average dewpoint

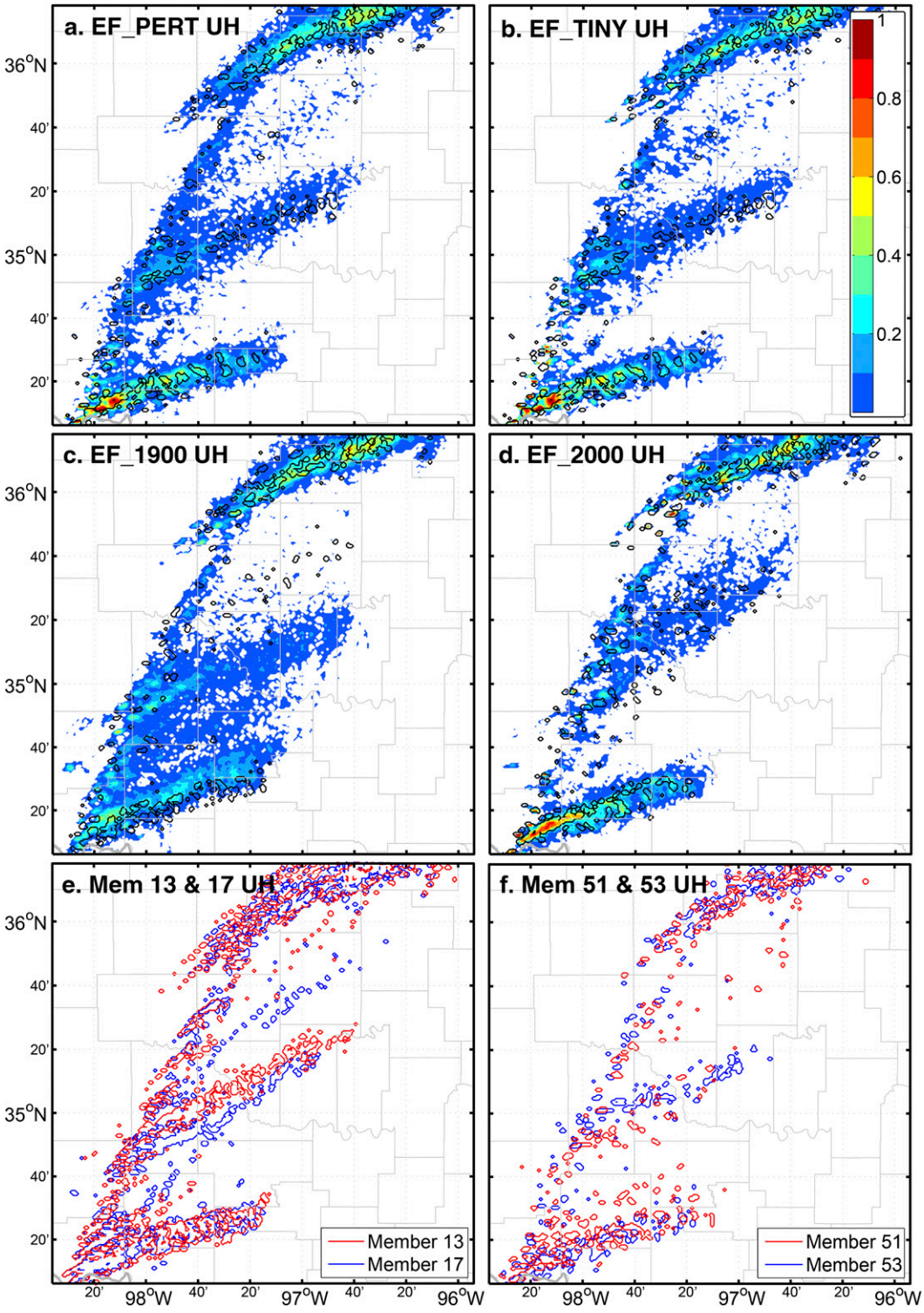

FIG. 6. Ensemble probability of $180\,m^2\,s^{-2}$ UH (shaded) throughout the entire forecast for (a) EF_PERT, (b) EF_TINY, (c) EF_1900, and (d) EF_2000, and $180\,m^2\,s^{-2}$ UH isolines of (e) members 13 and 17, and (f) members 51 and 53 of EF_PERT. Black lines in (a)–(d) are $180\,m^2\,s^{-2}$ UH isolines of (a),(b) CNTL_17Z; (c) CNTL_19Z; and (d) CNTL_20Z.

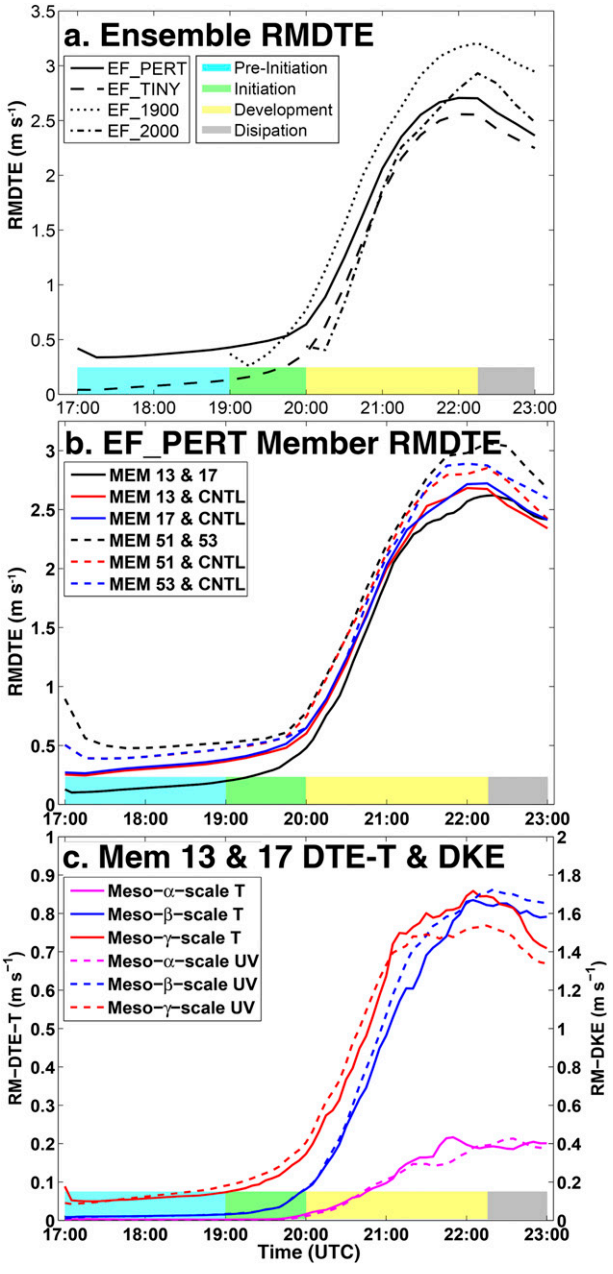

FIG. 7. (a) Ensemble-averaged RMDTE of EF_PERT (solid), EF_TINY (dashed), EF_1900 (dotted), and EF_2000 (dotted-dashed). (b) Domain-averaged RMDTE between members 13 and 17 (black solid), mem 13 and CNTL_17Z (red solid), member 17 and CNTL_17Z (blue solid), members 51 and 53 (black dashed), member 51 and CNTL_17Z (red dashed), and member 53 and CNTL_17Z (blue dashed). (c) Scale decomposition of DTE-T and DKE between members 13 and 17 with magnitude of DTE-T on the left y axis and DKE on the right y axis. Color bands along the x axis of each panel marked different stages during the simulation as indicated in (a).

temperature (T_d) in the lowest 1 km AGL, which changed nearly 10°C in less than 100 km (Fig. 8a) prior to CI. The isodrosotherms of the ensemble mean coincided well with those of CNTL_17Z. Larger values of ensemble spread of T_d were mostly located in the northwest region where T_d was lower than 13°C, while in the moist region, especially where 0–1-km T_d exceeded 20°C, differences in dewpoint temperatures among ensemble members were much smaller (ensemble spread < 0.5°C). Small differences between ensemble members and CNTL_17Z in the moist side of the dryline were revealed by both collocated isodrosotherms and small ensemble spread, implying that the ensemble perturbations had a minor impact on low-level moisture in this region prior to CI.

Similar results occurred for the fields of environmental instability and convective inhibition. Extreme values of most-unstable CAPE (MUCAPE) exceeding 4000 J kg^{-1} appeared in both CNTL_17Z and ensemble members, although there were larger ensemble spread values concentrated in more stable regions with MUCAPE below 4000 J kg^{-1} (Fig. 8b). Values of most-unstable convective inhibition (MUCIN) were below 0.5 J kg^{-1} in the high-instability, high-moisture region, while differences of MUCIN among ensemble members increased in the drier region (Fig. 8c). At the same time, LFC heights lowered to around 1000 m AGL in locations where convection first initiated, with few differences seen between ensemble members and CNTL_17Z (Fig. 8d).

These results suggest that to the east of the dryline where environmental conditions were favorable for CI, the impact of the initial errors on the environmental convective conditions was small. Thus, different ensemble members were equally favorable for CI and locations of the resultant convective storms were primarily determined by local maxima of updraft. Since these triggering mechanisms were turbulent and less predictable, they resulted in seemingly randomly distributed early convection in the ensemble members (see e.g., locations of strong convection to the north of the Oklahoma–Texas boarder at 2000 UTC from different ensemble members in Fig. 2). This difficulty in accurate prediction of CI is also discussed in section 5.

c. *Development stage of storms*

It is known that the propagation and organization of isolated convective storms are influenced by various dynamic and thermodynamic factors ranging from external environmental influences to internal storm structure (e.g., Rotunno and Klemp 1982; Weisman and Klemp 1982, 1984; Klemp 1987; Davies-Jones

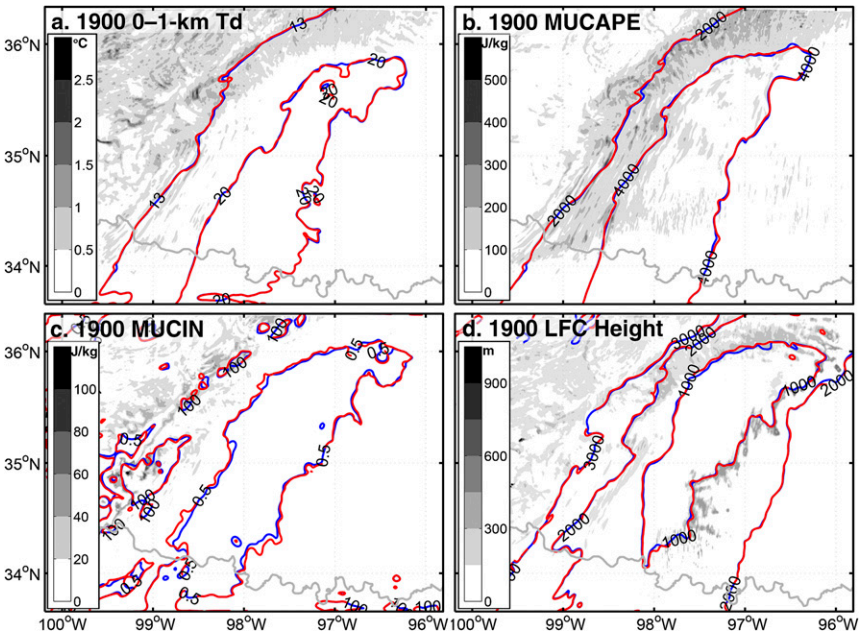

FIG. 8. Environmental convective conditions of (a) 13° and 20°C 0–1-km mass-weighted average isodrosotherms; (b) 2000 and 4000 J kg^{-1} MUCAPE; (c) 0.5 and 100 J kg^{-1} MUCIN; and (d) 1000-, 2000-, and 3000-m LFC height AGL valid at 1900 UTC with red isolines representing CNTL_17Z and blue isolines representing ensemble mean of EF_PERT with nine-point smoothing. Also plotted with shading are ensemble spreads of the respective conditions.

2002; Zeitler and Bunkers 2005; Kirkpatrick et al. 2007; Markowski and Richardson 2010). The general characteristics of storm translation were examined for the whole ensemble; examining the impact of each factor on the development of the simulated storms in a member-by-member sense is impractical and beyond the scope of this study. Equivalent potential temperature (θ_e) at 2-m above ground level was used to represent the cold pools generated by evaporative cooling of convection-induced precipitation. The extent and temperature drop of the cold pools were related to the location and strength of the convective storms.

At 2000 UTC (Fig. 9a), the 2-m ensemble mean θ_e lacked any signature of cold pool existence, partly due to the smoothing effect of the ensemble mean and partly due to the precipitation just reaching the ground. However, there were small regions where the ensemble spread of θ_e exceeds 5 K, indicating that precipitation in some members had already produced strong cold pools. One hour later at 2100 UTC (Fig. 9b), cold pools were apparent even in the ensemble mean, with 5-K ensemble spread covering the entire central cold pool, and a larger spread of 10 K at the northern tips of the cold pools, indicating large uncertainty in either strength or extent of the cold pools in ensemble members.

At 2200 UTC (Fig. 9c), regions of 5-K θ_e ensemble spread had already formed into a contiguous band to the east of the convective storms. This band broadened at the end of the ensemble forecast (Fig. 9d), while the ensemble mean cold pool was much weaker than before (i.e., θ_e became higher) indicating an overall weakening of convective outflow. Another thin line of larger θ_e spread formed along the western edge of the cold pools at the end of the forecast (Fig. 9d), resulting from the sharp gradient of moisture between the dry air to the west and the westward expanding cold pools.

In summary, after CI, differences in the strength and location of convection led to differences in the extent and temperature deficit of the accompanying cold pools, and the interactions between the cold pools and environment as well as impact from the cold pool itself resulted in different translations and organizational characteristics of the accompanying cold pools. This chain reaction, which magnified the small differences found in the convective cells during CI and subsequently influenced the behavior of thunderstorms in different ensemble members, is also widely acknowledged within the operational community. A detailed analysis of these processes is provided in section 5.

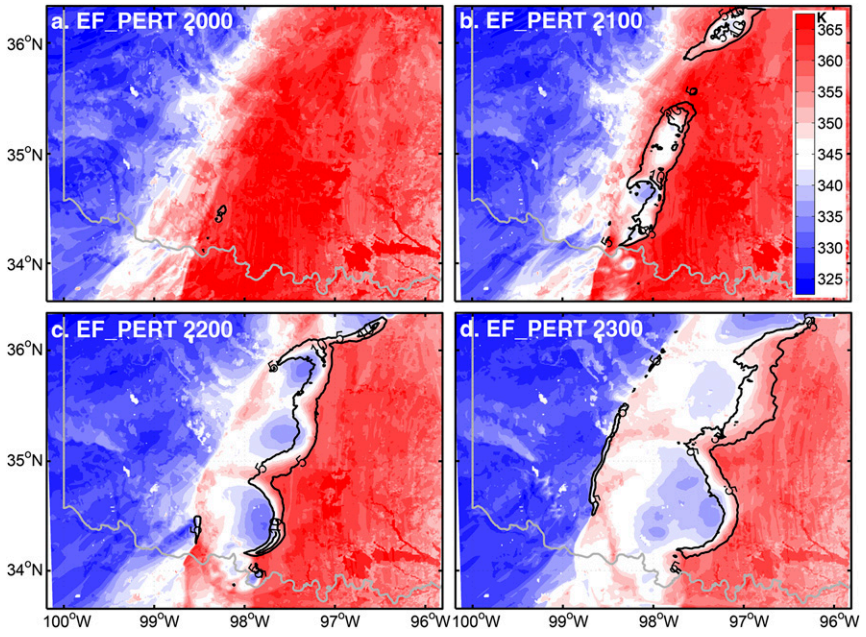

FIG. 9. Surface 2-m equivalent potential temperature (θ_e; shaded in K) and its ensemble spread (contoured every 5 K) for EF_PERT at (a) 2000, (b) 2100, (c) 2200, and (d) 2300 UTC.

4. Sensitivity of ensemble forecast to the magnitude and structure of initial perturbations

a. Uncertainties in the simulated storm of the EF_TINY ensemble

1) COMPARISON OF STORM FORECAST BETWEEN EF_TINY AND EF_PERT

One characteristic of limited intrinsic predictability is that no matter how much the initial errors are reduced, large uncertainty still occurs in the subsequent forecast (e.g., Zhang et al. 2003; Zhang and Sippel 2009; Melhauser and Zhang 2012). The EF_TINY ensemble was performed to examine the performance of ensemble forecast under reduced errors (statistics shown in Table 1). With ensemble spread narrowed by about one order of magnitude, the locations of earliest convection initiation were more concentrated in EF_TINY, with probabilities of 40-dBZ composite reflectivity collected into smaller areas and with higher values compared to EF_PERT (Figs. 3d,e); this indicates more confidence (less uncertainty) in the prediction of CI locations. This feature can also be seen at 2030 UTC when the coverage curve of EF_TINY was slightly flatter than EF_PERT (Fig. 5a). However, the probability areas rapidly spread out as convection developed. At 2100 and 2200 UTC, there were only minor differences between EF_TINY (Figs. 4d,e) and EF_PERT (Figs. 4a,b), and at 2300 UTC EF_TINY (Fig. 4f) became almost identical to EF_PERT (Fig. 4c). The 2130 and 2230 UTC coverage curve of EF_PERT and EF_TINY (Figs. 5b,c), as expected from visual comparison of ensemble probabilities, became very close to each other, although the fractional coverage of EF_TINY at threshold 0 was slightly smaller than EF_PERT. The similarity of the UH tracks and associated uncertainty between EF_PERT and EF_TINY (Figs. 6a,b) and their coverage curves of 180 $m^2 s^{-2}$ UH probability except for the slightly smaller value of EF_TINY at threshold 0 (Figs. 5d–f) confirmed their comparable lack of sufficient accuracy in predicting mesocyclone locations.

Owing to its much smaller initial errors, the differences between CNTL_17Z and the EF_TINY ensemble mean for moisture and instability fields prior to CI were even smaller than those between CNTL_17Z and the EF_PERT ensemble mean, as well as the ensemble spread of EF_TINY throughout the entire model domain (not shown). Similar to the characteristics in 40-dBZ composite reflectivity probability, the smaller ensemble spread and smaller temperature deficits of ensemble mean cold pool during CI and early development in EF_TINY quickly enlarged and EF_TINY became almost identical to EF_PERT in terms of both ensemble mean and ensemble spread of surface θ_e (not shown), indicating that the forecast divergence for thermodynamic fields, and associated convective storm characteristics, was almost indistinguishable

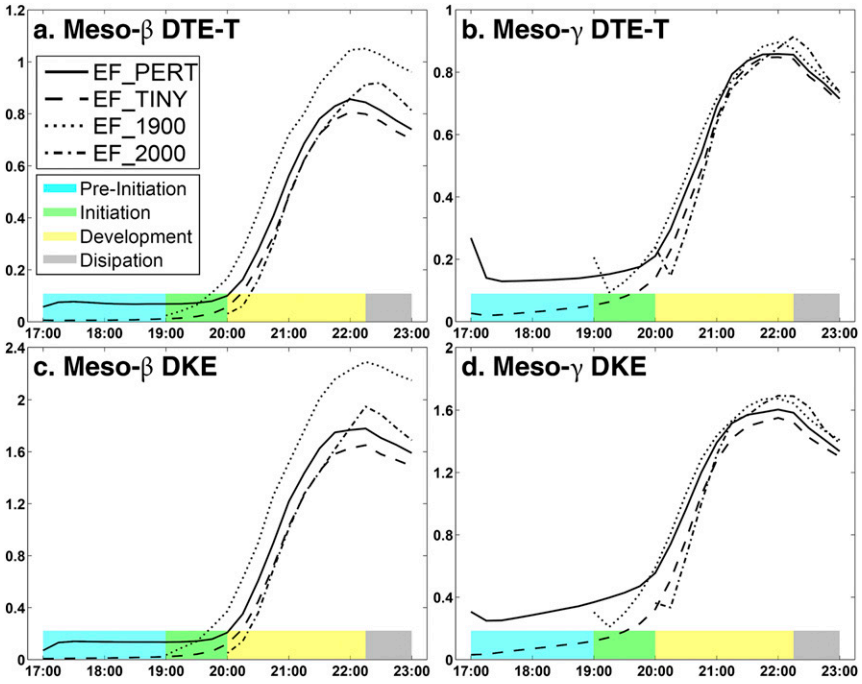

FIG. 10. Scale decomposition of (a),(b) DTE-T and (c),(d) DKE into (a),(c) meso-β and (b),(d) meso-γ scales of EF_PERT (solid), EF_TINY (dashed), EF_1900 (dotted), and EF_2000 (dotted–dashed). Color bands along the x axis of each panel marked different stages during the simulation as indicated in (a). Meso-α scale is omitted because the model domain is unable to resolve much wave lengths in that scale.

between the EF_PERT and EF_TINY. This loss of forecast accuracy in EF_TINY was also revealed in its RMDTE. At forecast initialization the RMDTE of EF_TINY was one order of magnitude smaller than EF_PERT (Fig. 7a), owing to the ensemble perturbation method. However, a more rapid increase than in EF_PERT occurred during CI (1900–2000 UTC), and shortly after CI RMDTE of EF_PERT and EF_TINY were almost identical. How ensemble errors evolved in different scales is examined in the following scale analyses.

2) ERROR GROWTH IN DIFFERENT SCALES WITH RESPECT TO INITIAL ERROR

The temperature component of DTE (DTE-T) and the wind component, difference kinetic energy (DKE), were further decomposed into meso-β and meso-γ scales according to Orlanski (1975). Figure 10 shows the changes of RMDTE-T and RMDKE at different scales with respect to integration times. For EF_PERT, it is interesting that only DKE in the meso-γ (Fig. 10d) scale experienced a persistent increase before 2000 UTC, whereas all other components of DTE at different scales remained almost unchanged during this 3-h period. After 2000 UTC, energy norms experienced a rapid increase at meso-β and meso-γ scales. However, both energy norms of temperature and winds for the meso-γ scale (Figs. 10b,d) stopped increasing after around 2100 UTC, while for the meso-β scale they increased until 2215 UTC (Figs. 10a,c) when the total RMDTE reached its maximum (Fig. 7a). This phenomenon suggests that errors in the meso-γ scale were saturated[2] and unable to further increase after about 2100 UTC.

For EF_TINY, both DTE-T and DKE in the meso-γ scale showed a persistent increase even before 2000 UTC (Figs. 10b,d). They also increased in the meso-β scale (Figs. 10a,c), although these increases started after 1800 UTC, which was later than the increases of their corresponding meso-γ-scale counterparts that started at the beginning of the simulations. This delay might be attributed to the upscale growth of errors. Considering

[2] Error saturation refers to when the difference energy (error or noise) at a given scale among ensemble members (or between truth and ensemble) reaches a magnitude that is comparable to the reference energy (truth or signal), after which the error at this scale ceases to grow any further since all the signal has been lost.

that there was no convection at this time, convection was not necessary for the upscale growth of errors. The different error growth rates before and after 2000 UTC confirmed the different error growth mechanisms with and without deep moist convection as found by Zhang et al. (2007), Hohenegger and Schär (2007a, b), and Selz and Craig (2015). After 2100 UTC, DTE-T and DKE of EF_TINY in the meso-γ scales reached almost identical values as those in EF_PERT, while in the meso-β scales they kept increasing until reaching their maxima at 2215 UTC. The same values of DTE-T and DKE in the meso-γ scale of both EF_PERT and EF_TINY after 2100 UTC confirmed that the errors were saturated in this scale at that time for this case. This phenomenon of error saturation at similar values regardless of the magnitude of initial errors was already presented in various studies (Hohenegger and Schär 2007a, b; Bei and Zhang 2007; Melhauser and Zhang 2012; Selz and Craig 2015). Furthermore, in a sensitivity ''fake dry'' experiment that excluded latent heat release associated with microphysics schemes, increases of DTE-T and DKE at all scales almost completely stagnated (not shown), suggesting the crucial role of moist processes in storm-scale rapid error growth.

b. *Influence of perturbing initial conditions at different times*

Ensemble spreads of EF_1900 and EF_2000 were a little smaller than those of EF_PERT at initialization (Table 1). However, the maximum deviations of perturbations of EF_1900 and EF_2000 from their respective ensemble mean were several times larger than in EF_PERT (Table 1), which was associated with sampling of the ongoing convection at the perturbed times. Because of these large uncertainties, the divergence of simulated storms developed rapidly. In just 2 h after initialization [i.e., 2100 UTC for EF_1900 (Fig. 4g) and 2200 UTC for EF_2000 UTC (Fig. 4k)], the probability of 40-dBZ reflectivity of these two ensembles became similar to EF_PERT.

Coverage curves further showed the similarity between EF_1900, EF_2000, and EF_PERT. At 2030 UTC (Fig. 5a), coverage curve of EF_2000 was quite flat since it has only integrated for 30 min, while coverage curve of EF_1900 was already almost identical to the EF_PERT curve and so were their curves 1 h later at 2130 UTC (Fig. 5b). The slope of EF_2000 curve at 2130 UTC, similar to the EF_TINY curve, was slightly flatter than EF_1900 and EF_PERT curves, indicating slightly less divergent storm locations. The similarity in coverage curves continued throughout the integration (Fig. 5c), with EF_1900 and EF_2000 showing slightly smaller values at lower thresholds and comparable values at higher thresholds. Coverage curves of 180 $m^2 s^{-2}$ UH showed similar characteristics: except for threshold 0, curves of EF_PERT, EF_1900, and EF_2000 were almost identical (Figs. 5d–f). At threshold 0, the value of the UH coverage curve of EF_1900 and EF_2000 was slightly larger than value of EF_PERT, indicating the slightly larger spread in UH tracks for these two ensembles as shown in Figs. 6c and 6d.

Although generally similar to EF_PERT and EF_TINY, the RMDTE evolution of EF_1900 and EF_2000 had some unique characteristics. One of the most distinct features was that rapid RMDTE increase occurred immediately after ensemble initialization (Fig. 7a). This was especially apparent in EF_1900 during CI stage that RMDTE increased rapidly, almost comparable to subsequent error growth during development of the thunderstorms after 2000 UTC, and its RMDTE was the largest among all four ensembles (Fig. 7a). When RMDTE of EF_1900 and EF_2000 were decomposed into different scales, DTE-T and DKE of all ensembles in meso-γ scales almost coincided with each other with an apparent saturation after 2100 UTC (Figs. 10b,d). On the other hand, the faster initial increase before 2000 UTC and resulting larger RMDTE of EF_1900 were primarily contributed by error growth in comparably larger scales (Figs. 10a,c).

Unlike other ensembles in which higher ensemble probabilities were generally collocated with their respective reference deterministic forecast, the EF_1900 was unique in that its ensemble probabilities drifted away. This disagreement was revealed in both 40-dBZ composite reflectivity, especially at longer forecast lead times (Figs. 4h,i) and 180 $m^2 s^{-2}$ UH (Fig. 6c). Furthermore, in the UH probability tracks (Fig. 6c), the higher probability of UH not only occurred more than 0.5° to the south of UH track predicted by CNTL_19Z, but also formed into a less-clear track between the track originated around 35°N and the southernmost track, which was not produced in any other ensembles. This mismatch between the probabilistic forecast and the deterministic forecast in EF_1900 confirmed the large uncertainties associated with CI processes and explained the reason that severe weather forecast paradigms such as ''warn-on-forecast'' focus on prediction of thunderstorms after they form. It also indicates that the performance and forecast accuracy of ensemble prediction systems might be sensitive to the initial perturbations.

5. Uncertainties in the simulated storm between two specific members

To examine how tiny initial differences affected convective storms in different ensemble members, RMDTE between all pairs of EF_PERT members was calculated, then the two members with the largest RMDTE increase between 1715 and 2215 UTC, members 13 and 17 (0.105 to 2.62 m s^{-1}), were selected for closer evaluation. Another two members, 51 and 53, were used as additional representations of ensemble divergence. RMDTE between members 51 and 53 at 1900 UTC was 0.524 m s^{-1}, which was close to the largest RMDTE at that time (0.526 m s^{-1}), while RMDTE between members 13 and 17 at that time was 0.199 m s^{-1}, close to the smallest RMDTE of 0.182 m s^{-1}. Members 13 and 17 were rerun to obtain a higher temporal resolution of 5 min, and their statistics at 1705 UTC are shown in Table 1.

Figure 11 shows the composite reflectivity of these four simulations. At 2000 UTC, there were only minor differences in members 13 and 17 (Figs. 11a1 and 11b1), while apparent differences occurred between member 51 and 53 (Figs. 11c1 and 11d1) as a consequence of their larger RMDTE at 1900 UTC. Differences between members 13 and 17 became clear at 2100 UTC where in member 13 the storms were still splitting (Fig. 11a2) and in member 17 the splitting was almost finished and individual storms could be easily identified (Fig. 11b2). On the other hand, a huge mismatch in storm location occurred between members 51 and 53 (Figs. 11c2 and 11d2). Storm merging occurred in the following hour. At 2200 UTC, the merger in member 17 almost totally dissipated (Fig. 11b3) in contrast with the storm in member 13 that was still strong (Fig. 11a3). The longer and slightly northern UH tracks in member 13 compared with member 17 were associated with this storm (Fig. 6e), confirming the longer duration of this storm in member 13 along with location separation from its counterpart in member 17. Member 51 experienced a similar dissipated merger storm as happened in member 17, while the merger in member 53 maintained for a longer time (Figs. 11c3 and 11d3). The UH tracks also highlighted corresponding differences in thunderstorm maintenance (Fig. 6f).

a. *Scale, altitude, and time evolution of RMDTE between ensemble members*

RMDTE between members 13/17 and CNTL_17Z (red and blue solid lines, respectively, in Fig. 7b) were almost identical to each other throughout the simulation, and were also close to RMDTE between these two members (black solid lines). This close resemblance also occurred between members 51/53 and CNTL_17Z (dashed lines). It should be noted that, although RMDTE between members 51 and 53 were much larger than between members 13 and 17 (0.563 vs 0.105 m s^{-1} at 1715 UTC), their error growth rates during storm development (2000–2100 UTC) were comparable and eventually reached similar maximum values (3.06 vs 2.62 m s^{-1} at 2215 UTC), a characteristic observed previously among different ensemble forecasts.

During the pre-CI stage, DTE-T and DKE in all scales showed small but persistent increases, and the greatest increase came from DKE in the meso-γ scale (Fig. 7c). Their vertical distributions indicate that before 1800 UTC, error growth in meso-γ scale were almost completely concentrated in the lowest 3 km AGL (i.e., the PBL; Figs. 12a,c). Although errors in the meso-β scale showed increase throughout all vertical levels (Figs. 12b,d), their influence on error growth were limited because of their smaller magnitude. After 1800 UTC, error growth in the meso-γ scale started to spread throughout the entire troposphere, especially DKE in the midtroposphere at times close to CI (Figs. 12a,c), which might have resulted from developing midlevel mesocyclones.

After 1900 UTC, DKE showed much greater increase than DTE-T, especially within the troposphere (Figs. 12e–h). Although domain-averaged DKE were generally twice the values of DTE-T (Fig. 7c), this ratio would become larger if only troposphere were considered (cf. Fig. 12e vs Fig. 12g, or Fig. 12f vs Fig. 12h), further suggesting the mesocyclone-driven nature of the thunderstorms. Besides, scale-decomposed DKE also contained scale-dependent structure. In the meso-γ scale, DKE increased almost homogeneously throughout the entire troposphere except for levels near surface resulting from midlevel mesocyclones (Fig. 12g), while in the meso-β scale, two apparent peaks occurred around tropopause and near surface, respectively, with smaller values in the midtroposphere (Fig. 12h), which was similar to the RMDTE evolution in the bow echo event of Melhauser and Zhang (2012, their Fig. 10).

b. *Physical processes lead to forecast bifurcation*

Since error growth before CI might be associated with the turbulent nature of this event, Fig. 13 shows TKE, bulk Richardson number (BRN), and the relative increase of DKE normalized by its values at 1705 UTC of member 13. Apparent increase in TKE occurred during the 2 hours before CI; larger TKE primarily concentrated in regions extending from 34°N, 99°W to 35°N, 98°W (Fig. 13a) where environmental conditions were most favorable for CI (Fig. 8) and later CI occurred. Low values of BRN (indicating larger vertical wind

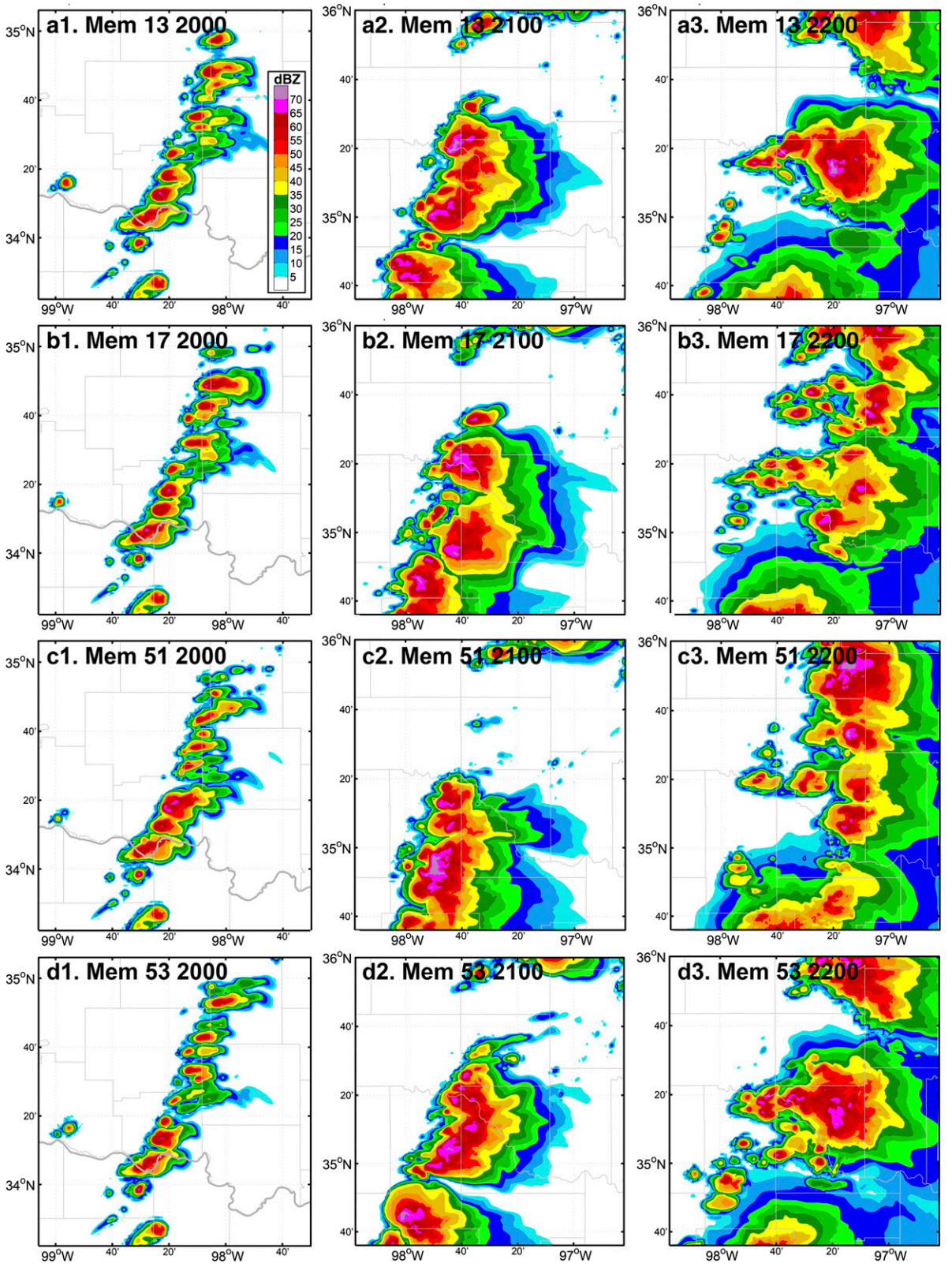

FIG. 11. Composite reflectivity of member (a) 13, (b) 17, (c) 51, and (d) 53 of EF_PERT at (left) 2000, (middle) 2100, and (right) 2200 UTC.

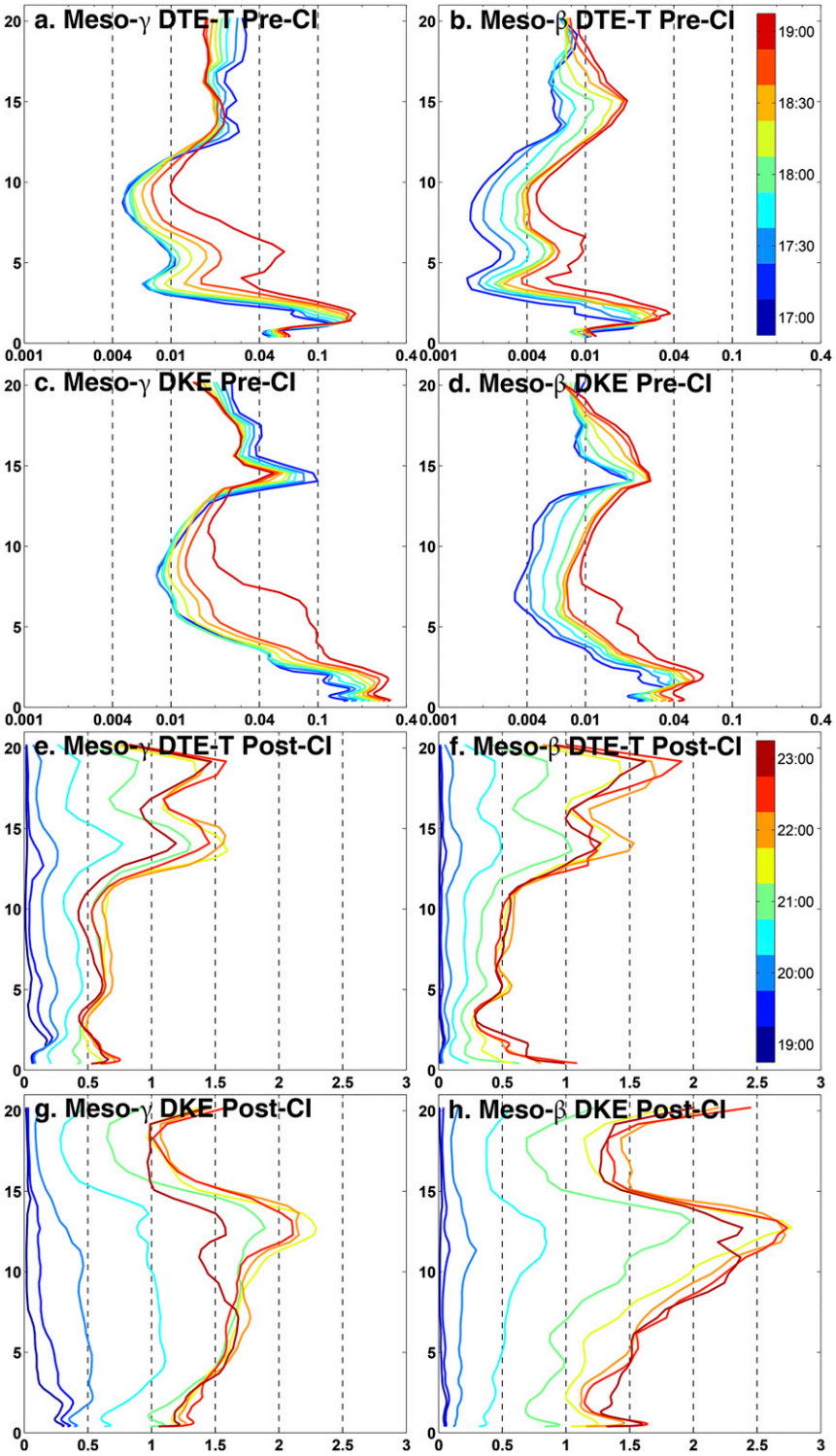

FIG. 12. Scale-decomposed time evolution of DTE-T and DKE between members 13 and 17. (a)–(d) Pre-CI stage before 1900 UTC [time of each color presented in (b)], and (e)–(h) are post-CI stage after 1900 UTC [time presented in (f)]. The first and third rows are DTE-T, and the second and fourth rows are DKE; (left) meso-γ scale and (right) meso-β scale.

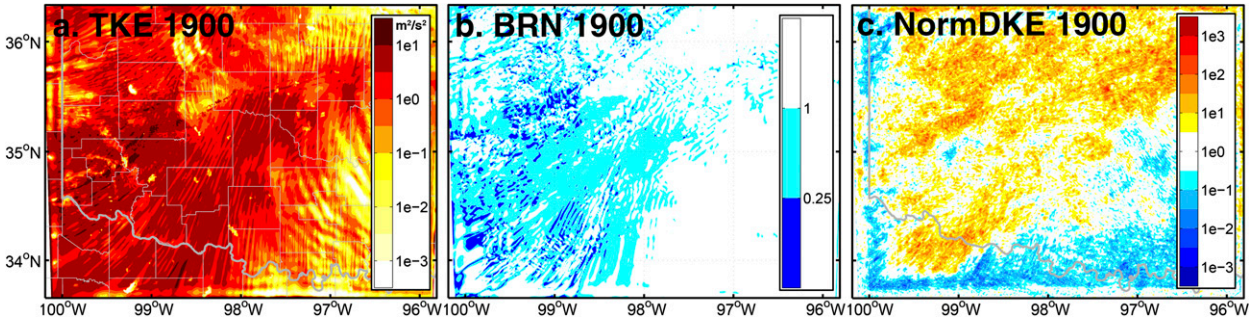

FIG. 13. (a) TKE ($m^2 s^{-2}$), (b) BRN calculated as BRN = $(g/T_v)[\Delta\theta_v\Delta_z/(\Delta u)^2 + (\Delta v)^2]$, where $g = 9.81\ m^2 s^{-2}$ is the gravitational acceleration; T_v is mean absolute virtual temperature across a layer of thickness Δz; and $\Delta\theta_v$, Δu, and Δv are the absolute difference of virtual potential temperature and two components of horizontal wind across the same layer, respectively. (c) DKE increase normalized by values at 1705 UTC of member 13 at 1900 UTC. The plotted layer is the 20th level from surface (roughly 1.2 km AGL) for TKE and DKE, and BRN was calculated across the 19th and the 21st levels.

shear thus higher probability for turbulent rather than laminar flow) were located within and to the west of this high-TKE region (Fig. 13b). At the same time, increases of DKE were primarily concentrated in the PBL before CI (Fig. 12c) in regions where large TKE and low BRN occurred (Fig. 13c). This consistency between increases of DKE before CI and PBL turbulence suggest possible relationships between them.

When convection occurred, members 13 and 17 bifurcated through various processes. At 1925 UTC the horizontal coverage of their 40-dBZ reflectivity was very similar (Fig. 14a). A small difference in vertical extent of the main convective cores appeared 5 min later at 1930 UTC (Figs. 15b,e) although in horizontal coverage they were still indistinguishable (Fig. 14b). Apparent differences in new cell development were identified at 1935 UTC with member 17 containing more convective cores (Fig. 14c), which could be roughly regarded as the time that the two members began to drift apart from each other (denoted as t_0 hereafter). The locations of

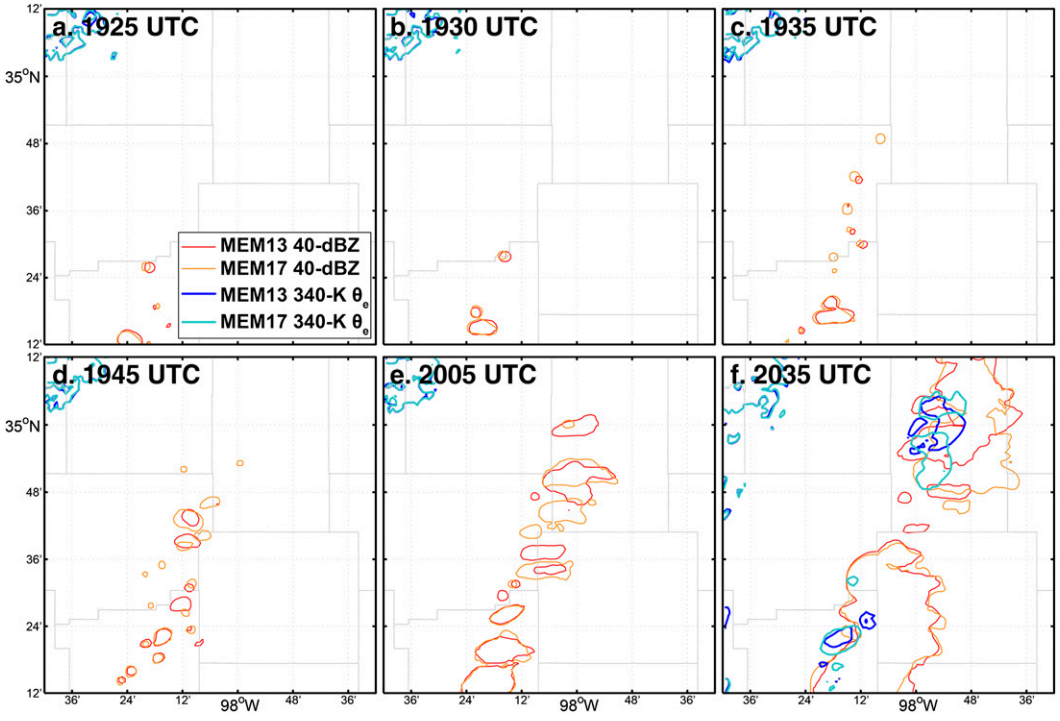

FIG. 14. Isolines of 40-dBZ composite reflectivity and 340-K surface 2-m θ_e of members 13 and 17 at (a) 1925, (b) 1930, (c) 1935, (d) 1945, (e) 2005, and (f) 2035 UTC.

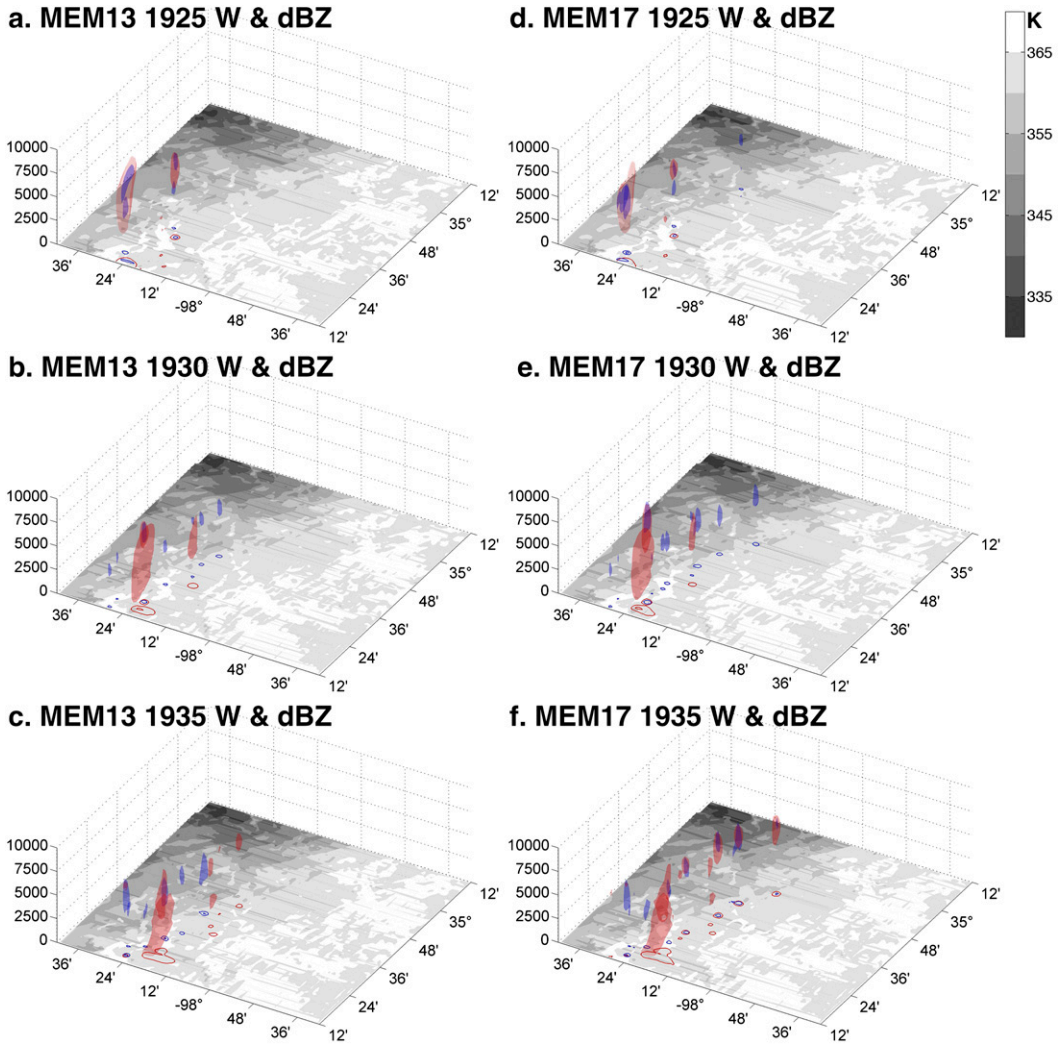

FIG. 15. Isosurfaces of 40-dBZ reflectivity (red) and 10 m s^{-1} updraft (blue), isolines of composite reflectivity (40 and 60 dBZ in red) and maximum updraft (every 10 m s^{-1} from 10 m s^{-1} in blue), and surface 2-m θ_e (shaded) of (a)–(c) member 13 and (d)–(f) member 17 at (a),(b) 1925; (c),(d) 1930; and (e),(f) 1935 UTC.

strong convective cores of the two members at t_0 were collocated with their respective updrafts (Figs. 15c,f), and these updrafts existed at $t_0 - 5$ when the 40 dBZ reflectivity fields were still almost identical (Figs. 14b and 15b,e). However, 10 min prior to t_0 (Figs. 14a and 15a,d), it was hard to determine where and when these updrafts might occur at 1930 UTC. Given the small spatial scales and the fast-evolving and turbulent nature of the dynamic fields, the updrafts were extremely difficult to predict even 10 min in advance.

Subsequent storm evolution and maintenance would be influenced by the environmental vertical wind shear (Weisman and Klemp 1982). Because of the pre-CI remnants of horizontal convective rolls, strong turbulence within the PBL and the surface outflow boundaries from nearby storms, there was large horizontal variability in surface wind fields and, therefore, in 0–6-km wind shear (Fig. 16). This situation led to wind shear changes as large as 10 m s^{-1} within a distance of several tens of kilometers. Thus, some of the storms dissipated shortly after initiation if they moved into regions of relatively weak wind shear, as can be observed in the southernmost convections of Figs. 15c and 15f, typical of single-cell storms with lifetimes less than 1 h. In contrast, updrafts of some other storms were accelerated through the interactions between the updraft and accompanying stronger wind shear (Rotunno and Klemp 1982) as well as due to the buoyancy generated by latent heat released from condensation of ascending air parcels. The indistinctive differences between the two simulations at t_0 (i.e., Fig. 14c) might be enlarged in as short as 10 min (Fig. 14d), resulting in large differences between

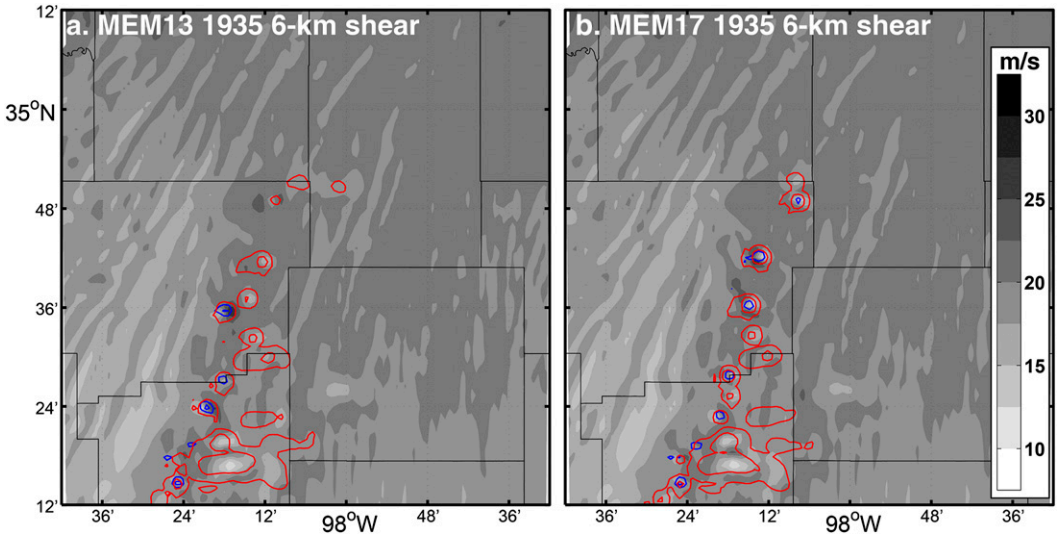

FIG. 16. The 0–6-km vertical wind shear (shaded every 2.5 m s^{-1}) and isolines of composite reflectivity (red every 20 dBZ from 20 dBZ) and vertical velocity (blue every 10 m s^{-1} from 10 m s^{-1}) of member (a) 13 and (b) 17 at 1935 UTC.

updrafts even at similar locations (cf. vertical velocity contours at the surfaces near 34°40′N, 98°12′W of Figs. 17a,d).

Divergence between convective cores was amplified within 30 min after t_0 (Fig. 14e) in that the strength and appearance of the updrafts and associated reflectivity became different (Figs. 17b,e). When cold pools formed due to evaporative cooling of convective precipitation after 2000 UTC (refer to Fig. 9a), they also played an important role in limiting the intrinsic predictability since they are closely related with the organization and development of convective storms. The differences in location, extent, and strength of reflectivity lead to corresponding alterations of cold pools, influencing subsequent development and organization of convection and further enlarging storm differences. As a result, in another 30 min (i.e., t_0 + 60), the differences in cold pools were quite apparent (Fig. 14f): two cold pools across 35°N were found in member 17 (Fig. 17f) indicating ongoing splitting process; in contrast, the storm development in member 13 had been slower (Fig. 17c), such that its surface cold pool was still unified. This phenomenon was consistent with (and faster than) Melhauser and Zhang (2012) in which the feedbacks associated with cold pools generated drastic differences within 1 or 2 h.

This accumulated effect of the cold pool feedbacks became even larger when splitting and merging processes occurred. In member 13, after the splitting of the original two storms, the middle two storms (marked as "S" and "N" in Figs. 18a and 18b) began approaching each other (Fig. 18a). When the leading edges of these cold pools (i.e., gust fronts) collided during the early stage of merging, new updrafts were produced (Fig. 18b). These updrafts persisted after merging (Fig. 18c) and the merged storm maintained its strength for a long time (marked as "M" in Figs. 18c and 18d) as did its cold pool (Fig. 18d).

Storm evolution in member 17 showed a different process. Storm interactions occurred 10 min earlier (Fig. 19a) in member 17 due to its faster development (Figs. 17e,f). Updrafts of the "S" storm in member 17 intruded into the rear side of the cold pool of the "N" storm (Fig. 19b). The updrafts became weak and disorganized and failed to maintain their intensity; simultaneously, the cold pool moved northwestward after merging and became dislocated from the updrafts (Fig. 19d), further disrupting the internal dynamics needed for the storm maintenance. The different storm evolutions found in members 13 and 17 revealed a drastic sensitivity of storm development to small alterations in timing, location, strength, and juxtaposition of individual storms, which agreed well with the idealized study of Bluestein and Weisman (2000). Similar processes occurred in member 51 (not shown) that also experienced a quick dissipation after storm merging (Fig. 11c3).

Two positive feedbacks located aloft and near the surface played a crucial rule in the growth of forecast errors associated with the storms. It should be noted that these feedbacks could alter the evolution of the

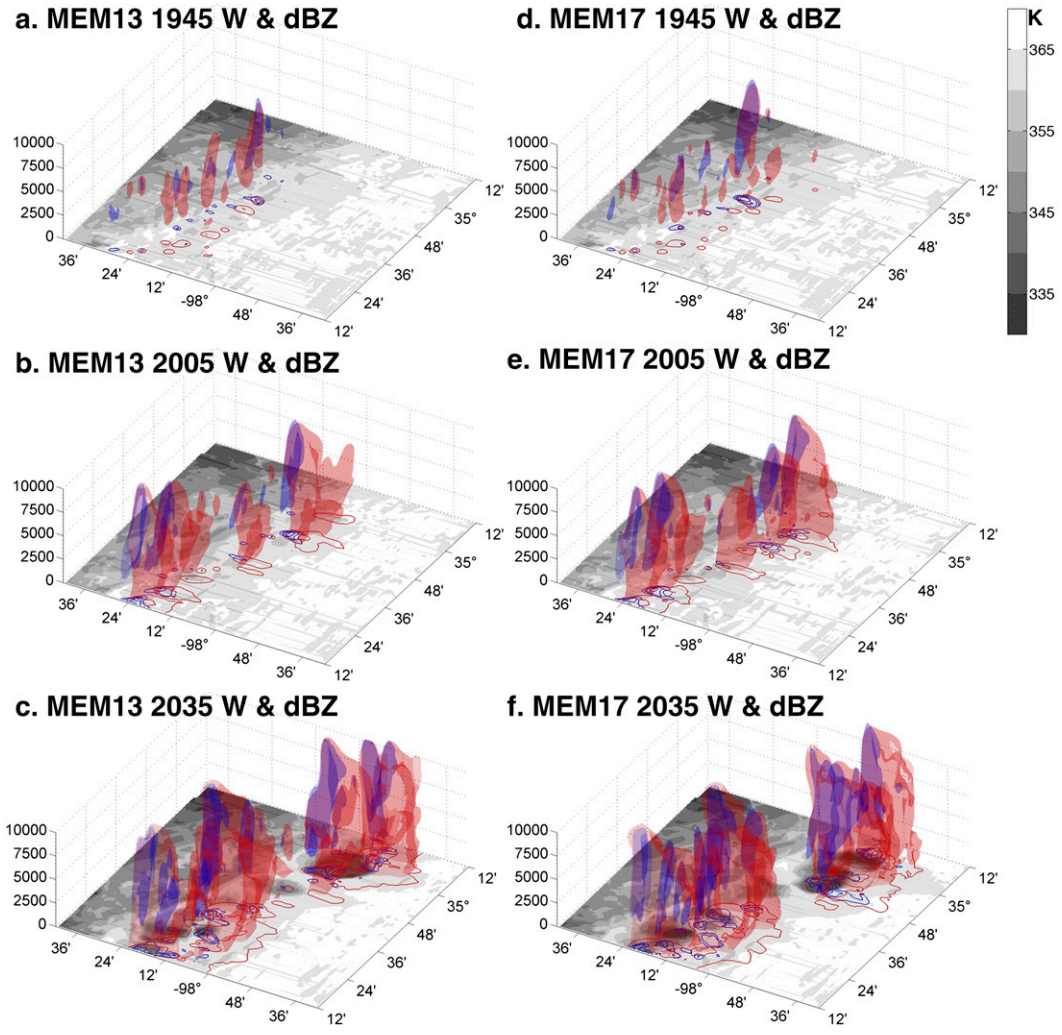

FIG. 17. As in Fig, 15, but for (a),(b) 1945; (c),(d) 2005; and (e),(f) 2035 UTC.

convective flows and consequently development and organization of the storms. Even with the initial differences between the two EF_PERT members being one order of magnitude smaller than errors of current observation instruments and global model analyses, results indicate that these differences could lead to failure in thunderstorm prediction. Our analyses of these two members highlighted the surprisingly large impact that limited intrinsic predictability might have on the prediction of severe thunderstorms in NWP models.

6. Conclusions

The time scale that storm-scale simulations are reliable and applicable is essential knowledge for the newly developed ''warn-on-forecast'' paradigm for severe weather warning, whereas how initial errors might grow in the storm scale is unknown. This work, focusing on the tornadic thunderstorm event in Oklahoma on 20 May 2013, examined the intrinsic predictability of this event via ensemble forecasts with the WRF Model in a convection-allowing horizontal resolution of 1 km, and explored the mechanisms of how tiny unobserved errors might influence the entire storm-scale forecast within a few hours.

Using a set of initial conditions that represent flow-dependent unobservable uncertainties, the control ensemble forecast (EF_PERT) showed two intrinsic predictability characteristics. On one hand, the overall quasi-contiguous line of severe convective storms across Oklahoma was well simulated in all ensemble members. Analysis of convective conditions shortly before convection initiation, including moisture, instability, and convective inhibition, confirmed that these conditions were nearly identical in all ensemble members,

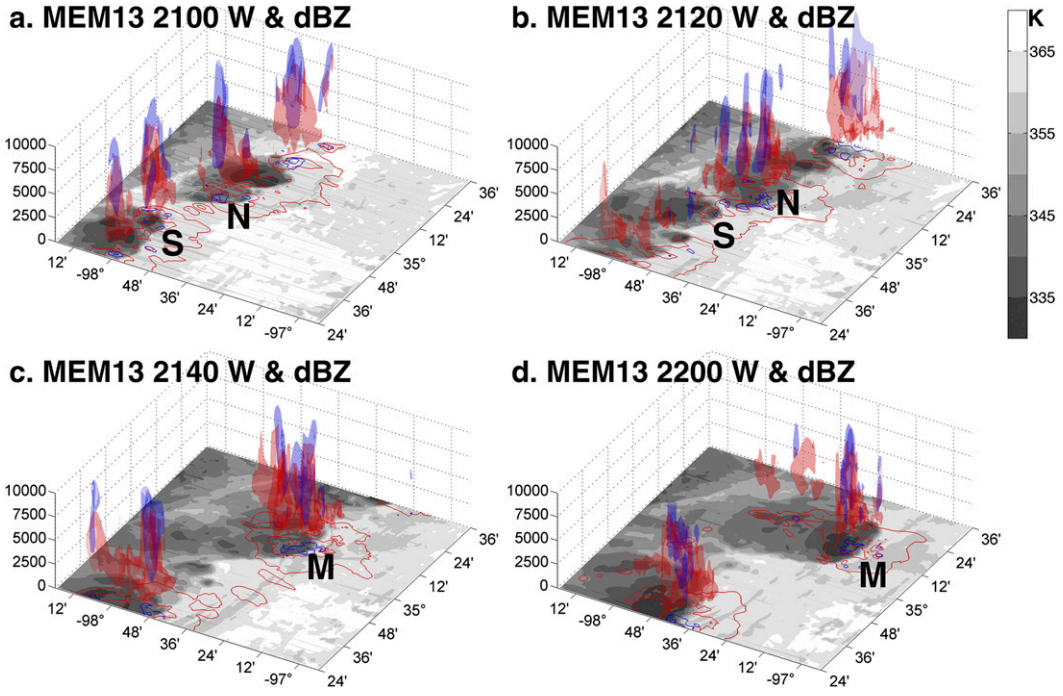

FIG. 18. Isosurfaces of 60-dBZ reflectivity (red) and 20 m s^{-1} updraft (blue), isolines of composite reflectivity (40 and 60 dBZ in red) and maximum updraft (every 20 m s^{-1} from 20 m s^{-1} in blue), and surface 2-m θ_e (shaded) of member 13 at (a) 2100, (b) 2120, (c) 2140, and (d) 2200 UTC. The S and N in (a),(b) indicate southern and northern cells that will be merged, respectively; and M in (c),(d) indicate the merger.

with ensemble mean closely following the reference CNTL_17Z simulation with small ensemble spreads. This similarity indicates that the environmental conditions were highly predictable for the spatiotemporal scale examined in the ensemble forecast for this event.

On the other hand, the location, morphology, and development of individual storms varied from member to member, and the strength and coverage of accumulated precipitation as well as the probability of mesocyclones contained large variations, suggesting a limited intrinsic storm-scale predictability. Furthermore, the uncertainties remained largely unchanged even when the initial perturbations were reduced by as much as 90% in the EF_TINY ensemble. Calculations of DTE confirmed the similar error magnitudes of EF_PERT and EF_TINY forecasts. Scale decompositions of DTE revealed error saturation and upscale growth, which can be amplified by deep moist convection. The structure and timing of initial perturbations might also influence the reliability of ensemble forecast in the storm scale as indicated by the difference between the EF_1900, EF_2000 and EF_PERT ensembles.

Members 13 and 17 of the EF_PERT ensemble were selected for detailed analysis of how their simulated thunderstorms became distinct from each other. Turbulence within the PBL played an important role in spreading and amplifying errors during the pre-CI stage. During the CI stage, the location and intensity of updrafts were hard to predict accurately; furthermore, large variability might occur in deep-layer vertical wind shear, making it hard to predict whether or not initiated storms will be long lived. For those long-lived thunderstorms, latent heat release during condensation may enhance the buoyancy and subsequently feed back to strengthen the updraft. Thus, randomly shifted updraft maxima during early convection initiation may lead to changes in both strength and extent of storm reflectivity and updrafts.

The development of storms is closely related to their accompanying cold pools and the interactions between cold pools, the updrafts, and the environment. More complex situations occur for storm splitting and merging: the juxtaposition of two thunderstorms before their merging is essential for the later development of the merger storm. In this study, the merged storm in member 13 was maintained, while in member 17 when the updrafts of one storm intruded upon the cold pool of the other storm from the rear side, the updrafts became disorganized and dissipated quickly after merging, and the merger storm dissipated.

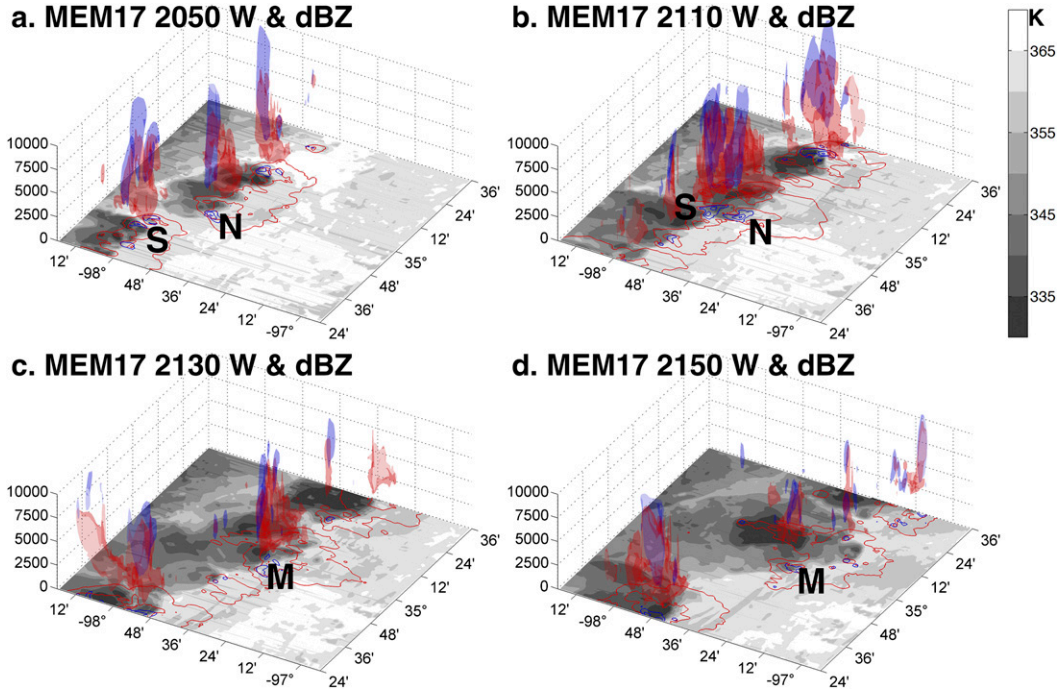

FIG. 19. As in Fig. 18, but for member 17.

In summary, although the convective phenomena in larger scales were highly predictable for this event, severe convective thunderstorms were found to be intrinsically highly unpredictable for forecast lead times within 3–6 h. Small alterations in the initial conditions might trigger updrafts randomly that could be rapidly magnified via interactions between updrafts, precipitation, and cold pools. Since errors might experience rapid upscale growth with the help of deep moist convection, a single deterministic forecast is not able to consider the impact of the uncertainty associated with the tiny unobserved initial errors, thus ensemble forecasts are needed for weather prediction at the storm scale. It should be noted that these processes and results were based upon one event and should not be much generalized; however, the fundamental dynamics and thermodynamics are likely universal, thus the limited intrinsic predictability of severe convective thunderstorms might not be restricted to this event. Furthermore, this study provides a guide to storm-scale predictions for how large the errors could be even providing nearly perfect knowledge of the atmosphere; results herein would be beneficial to application of ensemble-based forecast systems and interpretations of numerical simulations by human forecasters, thus contributing to the forecast and warning of severe weather in the future.

Acknowledgments. Discussions with Christopher Melhauser benefitted this work greatly. The authors would also like to thank the three anonymous reviewers for their valuable suggestions. Yunji Zhang is supported by the Ministry of Science and Technology of China Grant 2013CB430104, the Natural Science Foundation of China Grant 41375048, and the Chinese Scholarship Council (CSC). Fuqing Zhang is supported by the Office of Naval Research Grant N000140910526 and the National Science Foundation Grant AGS-1305798. David J. Stensrud is supported by the National Science Foundation Grant ATM-1230114. Zhiyong Meng is supported by the Natural Science Foundation of China Grants 41425018 and 41461164006. The simulations were performed on the Stampede supercomputer of the Texas Advanced Computing Center (TACC).

REFERENCES

Aksoy, A., D. C. Dowell, and C. Snyder, 2010: A multicase comparative assessment of the ensemble Kalman filter for assimilation of radar observations. Part II: Short-range ensemble forecasts. *Mon. Wea. Rev.*, **138**, 1273–1292, doi:10.1175/2009MWR3086.1.

Bei, N., and F. Zhang, 2007: Impacts of initial condition errors on mesoscale predictability of heavy precipitation along the mei-yu front of China. *Quart. J. Roy. Meteor. Soc.*, **133**, 83–99, doi:10.1002/qj.20.

Benjamin, S. G., G. A. Grell, J. M. Brown, and T. G. Smirnova, 2004: Mesoscale weather prediction with the RUC hybrid

isentropic-terrain-following coordinate model. *Mon. Wea. Rev.*, **132**, 473–494, doi:10.1175/1520-0493(2004)132<0473:MWPWTR>2.0.CO;2.

Bluestein, H. B., and M. L. Weisman, 2000: The interaction of numerically simulated supercells initiated along lines. *Mon. Wea. Rev.*, **128**, 3128–3149, doi:10.1175/1520-0493(2000)128<3128:TIONSS>2.0.CO;2.

Brotzge, J., and W. Donner, 2013: The tornado warning process: A review of current research, challenges, and opportunities. *Bull. Amer. Meteor. Soc.*, **94**, 1715–1733, doi:10.1175/BAMS-D-12-00147.1.

Bryan, G. H., J. C. Wyngaard, and J. M. Fritsch, 2003: Resolution requirements for the simulation of deep moist convection. *Mon. Wea. Rev.*, **131**, 2394–2416, doi:10.1175/1520-0493(2003)131<2394:RRFTSO>2.0.CO;2.

Burghardt, B. J., C. Evans, and P. J. Roebber, 2014: Assessing the predictability of convection initiation in the Hugh Plains using an object-based approach. *Wea. Forecasting*, **29**, 403–418, doi:10.1175/WAF-D-13-00089.1.

Chou, M.-D., and M. J. Suarez, 1994: An efficient thermal infrared radiation parameterization for use in general circulation models. NASA Tech. Memo, NASA, 84 pp.

Cintineo, R. M., and D. J. Stensrud, 2013: On the predictability of supercell thunderstorm evolution. *J. Atmos. Sci.*, **70**, 1993–2011, doi:10.1175/JAS-D-12-0166.1.

Clark, A. J., and Coauthors, 2012: An overview of the 2010 Hazardous Weather Testbed experimental forecast program Spring Experiment. *Bull. Amer. Meteor. Soc.*, **93**, 55–74, doi:10.1175/BAMS-D-11-00040.1.

Coleman, T. A., K. R. Knupp, J. Spann, J. B. Elliott, and B. E. Peters, 2011: The history (and future) of tornado warning dissemination in the United States. *Bull. Amer. Meteor. Soc.*, **92**, 567–582, doi:10.1175/2010BAMS3062.1.

Coniglio, M. C., K. L. Elmore, J. S. Kain, S. J. Weiss, M. Xue, and M. L. Weisman, 2010: Evaluation of WRF model output for severe weather forecasting from the 2008 NOAA Hazardous Weather Testbed Spring Experiment. *Wea. Forecasting*, **25**, 408–427, doi:10.1175/2009WAF2222258.1.

Davies-Jones, R. P., 2002: Linear and nonlinear propagation of supercell storms. *J. Atmos. Sci.*, **59**, 3178–3205, doi:10.1175/1520-0469(2003)059<3178:LANPOS>2.0.CO;2.

Dawson, D. T., II, L. J. Wicker, E. R. Mansell, and R. L. Tanamachi, 2012: Impact of the environmental low-level wind profile on ensemble forecasts of the 4 May 2007 Greensburg, Kansas, tornadic storm and associated mesocyclones. *Mon. Wea. Rev.*, **140**, 696–716, doi:10.1175/MWR-D-11-00008.1.

Doswell, C. A., H. E. Brooks, and R. A. Maddox, 1996: Flash flood forecasting: An ingredients-based methodology. *Wea. Forecasting*, **11**, 560–581, doi:10.1175/1520-0434(1996)011<0560:FFFAIB>2.0.CO;2.

Durran, D. R., and M. Gingrich, 2014: Atmospheric predictability: Why butterflies are not of practical importance. *J. Atmos. Sci.*, **71**, 2476–2488, doi:10.1175/JAS-D-14-0007.1.

——, P. A. Reinecke, and J. D. Doyle, 2013: Large-scale errors and mesoscale predictability in Pacific Northwest snowstorms. *J. Atmos. Sci.*, **70**, 1470–1487, doi:10.1175/JAS-D-12-0202.1.

Gasperoni, N. A., M. Xue, R. D. Palmer, and J. Gao, 2013: Sensitivity of convective initiation prediction to near-surface moisture when assimilating radar refractivity: Impact tests using OSSEs. *J. Atmos. Oceanic Technol.*, **30**, 2281–2302, doi:10.1175/JTECH-D-12-00038.1.

Green, B. W., and F. Zhang, 2015: Numerical simulations of Hurricane Katrina (2005) in the turbulent gray zone. *J. Adv. Model. Earth Syst.*, **7**, 142–161, doi:10.1002/2014MS000399.

Grell, G. A., and D. Dévényi, 2002: A generalized approach to parameterizing convection combining ensemble and data assimilation techniques. *Geophys. Res. Lett.*, **29**, 1693, doi:10.1029/2002GL015311.

Hawblitzel, D. P., F. Zhang, Z. Meng, and C. A. Davis, 2007: Probabilistic evaluation of the dynamics and predictability of the mesoscale convective vortex of 10–13 June 2003. *Mon. Wea. Rev.*, **135**, 1544–1563, doi:10.1175/MWR3346.1.

Hohenegger, C., and C. Schär, 2007a: Atmospheric predictability at synoptic versus cloud resolving scales. *Bull. Amer. Meteor. Soc.*, **88**, 1783–1793, doi:10.1175/BAMS-88-11-1783.

——, and ——, 2007b: Predictability and error growth dynamics in cloud-resolving models. *J. Atmos. Sci.*, **64**, 4467–4478, doi:10.1175/2007JAS2143.1.

Johns, R. H., and C. A. Doswell, 1992: Severe local storms forecasting. *Wea. Forecasting*, **7**, 588–612, doi:10.1175/1520-0434(1992)007<0588:SLSF>2.0.CO;2.

Johnson, A., and X. Wang, 2013: Object-based evaluation of a storm-scale ensemble during the 2009 NOAA Hazardous Weather Testbed Spring Experiment. *Mon. Wea. Rev.*, **141**, 1079–1098, doi:10.1175/MWR-D-12-00140.1.

——, ——, F. Kong, and M. Xue, 2011a: Hierarchical cluster analysis of a convection-allowing ensemble during the Hazardous Weather Testbed 2009 Spring Experiment. Part I: Development of the object-oriented cluster analysis method for precipitation fields. *Mon. Wea. Rev.*, **139**, 3673–3693, doi:10.1175/MWR-D-11-00015.1.

——, ——, M. Xue, and F. Kong, 2011b: Hierarchical cluster analysis of a convection-allowing ensemble during the Hazardous Weather Testbed 2009 Spring Experiment. Part II: Ensemble clustering over the whole experiment period. *Mon. Wea. Rev.*, **139**, 3694–3710, doi:10.1175/MWR-D-11-00016.1.

——, and Coauthors, 2014: Multiscale characteristics and evolution of perturbations for warm season convection-allowing precipitation forecasts: Dependence on background flow and method of perturbation. *Mon. Wea. Rev.*, **142**, 1053–1073, doi:10.1175/MWR-D-13-00204.1.

Kain, J. S., and Coauthors, 2013: A feasible study for probabilistic convection initiation forecasts based on explicit numerical guidance. *Bull. Amer. Meteor. Soc.*, **94**, 1213–1225, doi:10.1175/BAMS-D-11-00264.1.

Karstens, C. D., and Coauthors, 2015: Evaluation of a probabilistic forecasting methodology for severe convective weather in the 2014 Hazardous Weather Testbed. *Wea. Forecasting*, **30**, 1551–1570, doi:10.1175/WAF-D-14-00163.1.

Kirkpatrick, J. C., E. W. McCaul Jr., and C. Cohen, 2007: The motion of simulated convective storms as a function of basic environmental parameters. *Mon. Wea. Rev.*, **135**, 3033–3051, doi:10.1175/MWR3447.1.

Klemp, J. B., 1987: Dynamics of tornadic thunderstorms. *Annu. Rev. Fluid Mech.*, **19**, 369–402, doi:10.1146/annurev.fl.19.010187.002101.

Lane, T. P., and J. C. Knievel, 2005: Some effects of model resolution on simulated gravity waves generated by deep, mesoscale convection. *J. Atmos. Sci.*, **62**, 3408–3419, doi:10.1175/JAS3513.1.

Leoncini, G., R. S. Plant, S. L. Gray, and P. A. Clark, 2010: Perturbation growth at the convective scale for CSIP IOP18. *Quart. J. Roy. Meteor. Soc.*, **136**, 653–670, doi:10.1002/qj.587.

Lorenz, E. N., 1963: Deterministic nonperiodic flow. *J. Atmos. Sci.*, **20**, 130–141, doi:10.1175/1520-0469(1963)020<0130:DNF>2.0.CO;2.

——, 1969: The predictability of a flow which possesses many scales of motion. *Tellus*, **21A**, 289–307, doi:10.1111/j.2153-3490.1969.tb00444.x.

——, 1982: Atmospheric predictability experiments with a large numerical model. *Tellus*, **34A**, 505–513, doi:10.1111/j.2153-3490.1982.tb01839.x.

——, 1996: Predictability—A problem partly solved. *Proc. Seminar on Predictability*, Reading, United Kingdom, ECMWF, 1–18.

Markowski, P., and Y. Richardson, 2010: *Mesoscale Meteorology in Midlatitudes*. Wiley-Blackwell, 407 pp.

Melhauser, C., and F. Zhang, 2012: Practical and intrinsic predictability of severe and convective weather at the mesoscales. *J. Atmos. Sci.*, **69**, 3350–3371, doi:10.1175/JAS-D-11-0315.1.

Mlawer, E. J., S. J. Taubman, P. D. Brown, M. J. Iacono, and S. A. Clough, 1997: Radiative transfer for inhomogeneous atmospheres: RRTM, a validated correlated-k model for the longwave. *J. Geophys. Res.*, **102**, 16 663–16 682, doi:10.1029/97JD00237.

Nakanishi, M., and H. Niino, 2009: Development of an improved turbulence closure model for the atmospheric boundary layer. *J. Meteor. Soc. Japan*, **87**, 895–912, doi:10.2151/jmsj.87.895.

Naylor, J., M. S. Gilmore, R. L. Thompson, R. Edwards, and R. B. Wilhelmson, 2012: Comparison of objective supercell identification techniques using an idealized cloud model. *Mon. Wea. Rev.*, **140**, 2090–2102, doi:10.1175/MWR-D-11-00209.1.

Orlanski, I., 1975: A rational subdivision of scales for atmospheric processes. *Bull. Amer. Meteor. Soc.*, **56**, 527–534.

Roebber, P. J., D. M. Schultz, B. A. Colle, and D. J. Stensrud, 2004: Toward improved prediction: High-resolution and ensemble modeling systems in operations. *Wea. Forecasting*, **19**, 936–949, doi:10.1175/1520-0434(2004)019<0936:TIPHAE>2.0.CO;2.

Rotunno, R., and J. B. Klemp, 1982: The influence of the shear-induced pressure gradient on thunderstorm motion. *Mon. Wea. Rev.*, **110**, 136–151, doi:10.1175/1520-0493(1982)110<0136:TIOTSI>2.0.CO;2.

Schaefer, J. T., 1986: Severe thunderstorm forecasting: A historical perspective. *Wea. Forecasting*, **1**, 164–189, doi:10.1175/1520-0434(1986)001<0164:STFAHP>2.0.CO;2.

Selz, T., and G. Craig, 2015: Upscale error growth in a high-resolution simulation of a summertime weather event over Europe. *Mon. Wea. Rev.*, **143**, 813–827, doi:10.1175/MWR-D-14-00140.1.

Skamarock, W. C., and Coauthors, 2008: A description of the Advanced Research WRF version 3. NCAR Tech. Note, NCAR/TN-475+STR, NCAR/MMM, 113 pp., doi:10.5065/D68S4MVH.

Snook, N., X. Ming, and Y. Jung, 2012: Ensemble probabilistic forecasts of a tornadic mesoscale convective system from ensemble Kalman filter analyses using WSR-88D and CASA radar data. *Mon. Wea. Rev.*, **140**, 2126–2146, doi:10.1175/MWR-D-11-00117.1.

Snyder, C., and F. Zhang, 2003: Assimilation of simulated Doppler radar observations with an ensemble Kalman filter. *Mon. Wea. Rev.*, **131**, 1663–1677, doi:10.1175//2555.1.

Stensrud, D. J., and J. Gao, 2010: Importance of horizontally inhomogeneous environmental initial conditions to ensemble storm-scale radar data assimilation and very short-range forecasts. *Mon. Wea. Rev.*, **138**, 1250–1272, doi:10.1175/2009MWR3027.1.

——, and Coauthors, 2009: Convective-scale warn-on-forecast system. *Bull. Amer. Meteor. Soc.*, **90**, 1487–1499, doi:10.1175/2009BAMS2795.1.

——, and Coauthors, 2013: Progress and challenges with Warn-on-Forecast. *Atmos. Res.*, **123**, 2–16, doi:10.1016/j.atmosres.2012.04.004.

Surcel, M., I. Zawadzki, and M. K. Yau, 2014: On the filtering properties of ensemble averaging for storm-scale precipitation forecasts. *Mon. Wea. Rev.*, **142**, 1093–1105, doi:10.1175/MWR-D-13-00134.1.

——, ——, and ——, 2015: A study on the scale dependence of the predictability of precipitation patterns. *J. Atmos. Sci.*, **72**, 216–235, doi:10.1175/JAS-D-14-0071.1.

Thompson, G., P. R. Field, R. M. Rasmussen, and W. D. Hall, 2008: Explicit forecasts of winter precipitation using an improved bulk microphysics scheme. Part II: Implementation of a new snow parameterization. *Mon. Wea. Rev.*, **136**, 5095–5115, doi:10.1175/2008MWR2387.1.

Van Sang, N., R. K. Smith, and M. T. Montgomery, 2008: Tropical-cyclone intensification and predictability in three dimensions. *Quart. J. Roy. Meteor. Soc.*, **134**, 563–582, doi:10.1002/qj.235.

Wang, H., T. Auligne, and H. Morrison, 2012: Impact of microphysics scheme complexity on the propagation of initial perturbations. *Mon. Wea. Rev.*, **140**, 2287–2296, doi:10.1175/MWR-D-12-00005.1.

Weckwerth, T. M., and D. B. Parsons, 2006: A review of convection initiation and motivation for IHOP_2002. *Mon. Wea. Rev.*, **134**, 5–22, doi:10.1175/MWR3067.1.

——, and Coauthors, 2004: An overview of the International H_2O Project (IHOP_2002) and some preliminary highlights. *Bull. Amer. Meteor. Soc.*, **85**, 253–277, doi:10.1175/BAMS-85-2-253.

Wei, J., and F. Zhang, 2014: Mesoscale gravity waves in moist baroclinic jet–front systems. *J. Atmos. Sci.*, **71**, 929–952, doi:10.1175/JAS-D-13-0171.1.

Weisman, M. L., and J. B. Klemp, 1982: The dependence of numerically simulated convective storms on vertical wind shear and buoyancy. *Mon. Wea. Rev.*, **110**, 504–520, doi:10.1175/1520-0493(1982)110<0504:TDONSC>2.0.CO;2.

——, and ——, 1984: The structure and classification of numerically simulated convective storms in directionally varying wind shears. *Mon. Wea. Rev.*, **112**, 2479–2498, doi:10.1175/1520-0493(1984)112<2479:TSACON>2.0.CO;2.

Wheatley, D. M., N. Yussouf, and D. J. Stensrud, 2014: Ensemble Kalman filter analyses and forecasts of a severe mesoscale convective system using different choices of microphysics schemes. *Mon. Wea. Rev.*, **142**, 3243–3263, doi:10.1175/MWR-D-13-00260.1.

Wilson, J. W., and R. D. Roberts, 2006: Summary of convective storm initiation and evolution during IHOP: Observational and modeling perspective. *Mon. Wea. Rev.*, **134**, 23–47, doi:10.1175/MWR3069.1.

Wu, D., Z. Meng, and D. Yan, 2013: The predictability of a squall line in South China on 23 April 2007. *Adv. Atmos. Sci.*, **30**, 485–502, doi:10.1007/s00376-012-2076-x.

Yussouf, N., E. R. Mansell, L. J. Wicker, D. M. Wheatley, and D. J. Stensrud, 2013: The ensemble Kalman filter analyses and forecasts of the 8 May 2003 Oklahoma City tornadic supercell storm using single- and double-moment microphysics schemes. *Mon. Wea. Rev.*, **141**, 3388–3412, doi:10.1175/MWR-D-12-00237.1.

——, D. C. Dowell, L. J. Wicker, K. H. Knopfmeier, and D. M. Wheatley, 2015: Storm-scale data assimilation and ensemble forecasts for the 27 April 2011 severe weather outbreak in Alabama. *Mon. Wea. Rev.*, **143**, 3044–3066, doi:10.1175/MWR-D-14-00268.1.

Zhang, D., and R. A. Anthes, 1982: A high-resolution model of the planetary boundary layer—Sensitivity tests and comparisons with SESAME-79 data. *J. Appl. Meteor.*, **21**, 1594–1609, doi:10.1175/1520-0450(1982)021<1594:AHRMOT>2.0.CO;2.

Zhang, F., and J. Sippel, 2009: Effects of moist convection on hurricane predictability. *J. Atmos. Sci.*, **66**, 1944–1961, doi:10.1175/2009JAS2824.1.

——, and D. Tao, 2013: Effects of vertical wind shear on the predictability of tropical cyclones. *J. Atmos. Sci.*, **70**, 975–983, doi:10.1175/JAS-D-12-0133.1.

——, C. Snyder, and R. Rotunno, 2002: Mesoscale predictability of the ''surprise'' snowstorm of 24–25 January 2000. *Mon. Wea. Rev.*, **130**, 1617–1632, doi:10.1175/1520-0493(2002)130<1617:MPOTSS>2.0.CO;2.

——, ——, and ——, 2003: Effects of moist convection on mesoscale predictability. *J. Atmos. Sci.*, **60**, 1173–1185, doi:10.1175/1520-0469(2003)060<1173:EOMCOM>2.0.CO;2.

——, A. M. Odins, and J. W. Nielsen-Gammon, 2006: Mesoscale predictability of an extreme warm-season precipitation event. *Wea. Forecasting*, **21**, 149–166, doi:10.1175/WAF909.1.

——, N. Bei, R. Rotunno, C. Snyder, and C. Epifanio, 2007: Mesoscale predictability of moist baroclinic waves: Convection-permitting experiments and multistage error growth dynamics. *J. Atmos. Sci.*, **64**, 3579–3594, doi:10.1175/JAS4028.1.

Zhang, Y., F. Zhang, D. J. Stensrud, and Z. Meng, 2015: Practical predictability of the 20 May 2013 tornadic thunderstorm event in Oklahoma: Sensitivity to synoptic timing and topographical influence. *Mon. Wea. Rev.*, **143**, 2973–2997, doi:10.1175/MWR-D-14-00394.1.

Zeitler, J. W., and M. J. Bunkers, 2005: Operational forecasting of supercell motion: Review and case studies using multiple datasets. *Natl. Wea. Dig.*, **29**, 81–97.